

A SPECTRAL METHOD FOR MULTI-VIEW SUBSPACE LEARNING USING THE PRODUCT OF PROJECTIONS

RENAT SERGAZINOV

Department of Statistics, Texas A&M University, College Station, TX

ARMEEN TAEB

Department of Statistics, University of Washington, Seattle, WA

IRINA GAYNANOVA*

Department of Biostatistics, University of Michigan, Ann Arbor, MI

ABSTRACT. Multi-view data provides complementary information on the same set of observations, with multi-omics and multimodal sensor data being common examples. Analyzing such data typically requires distinguishing between shared (joint) and unique (individual) signal subspaces from noisy, high-dimensional measurements. Despite many proposed methods, the conditions for reliably identifying joint and individual subspaces remain unclear. We rigorously quantify these conditions, which depend on the ratio of the signal rank to the ambient dimension, principal angles between true subspaces, and noise levels. Our approach characterizes how spectrum perturbations of the product of projection matrices, derived from each view’s estimated subspaces, affect subspace separation. Using these insights, we provide an easy-to-use and scalable estimation algorithm. In particular, we employ rotational bootstrap and random matrix theory to partition the observed spectrum into joint, individual, and noise subspaces. Diagnostic plots visualize this partitioning, providing practical and interpretable insights into the estimation performance. In simulations, our method estimates joint and individual subspaces more accurately than existing approaches. Applications to multi-omics data from colorectal cancer patients and nutrigenomic study of mice demonstrate improved performance in downstream predictive tasks.

1. INTRODUCTION

Multi-view data provides complementary information on the same set of observations, with multi-omics and multimodal sensor data being common examples. Since each data source or view is potentially high-dimensional, it is of interest to identify a low-dimensional representation of the signal and further distinguish whether the signal is shared (joint) across views or view-specific (individual). For example, in § 5.1, we consider colorectal cancer data with RNAseq and miRNA views. The goal is to identify joint signals from these two views and validate whether these signals predict cancer subtypes (Guinney et al., 2015).

Canonical correlation analysis (Hotelling, 1936) is a time-tested approach for finding associated signals across views, but it cannot distinguish individual signals. To address this limitation, many methods have been developed to explicitly model joint and individual signals (Van Deun et al., 2009; Lock et al., 2013; Zhou et al., 2015; Yang & Michailidis, 2016; Feng et al., 2018; Shu et al., 2019; Gaynanova & Li, 2019; Park & Lock, 2020; Murden et al., 2022; Prothero et al., 2024).

Despite significant methodological advances, a crucial theoretical question remains: when can joint and individual signals be reliably identified from multi-view data? To answer this question, we start with the

*Corresponding author: irinagn@umich.edu.

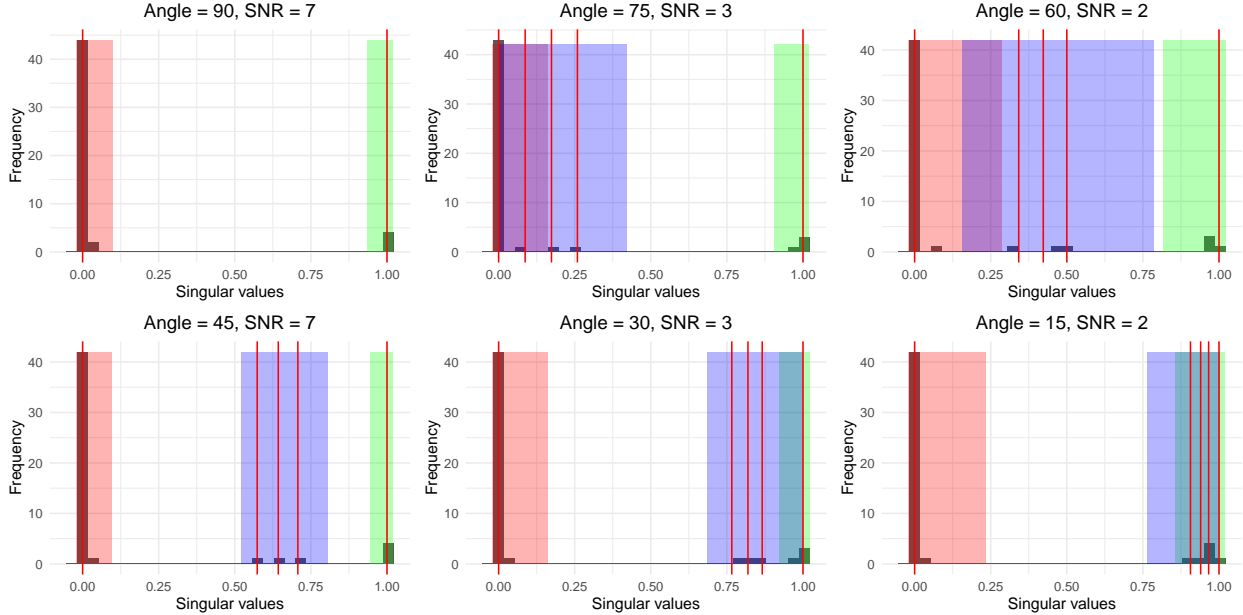


FIGURE 1. The alignment between the observed spectrum of the product of projections (grey histogram) and theoretical predictions from Theorem 3.1 (highlighted blocks) under varying angles between individual subspaces and signal-to-noise ratios (SNR). The theoretical intervals correspond to the **joint**, **non-orthogonal individual**, and **orthogonal individual and noise** components. The vertical **red** lines show the singular values in the noiseless setting.

two-view case and adopt the definition of joint and individual signal subspaces following Lock et al. (2013); Zhou et al. (2015); Feng et al. (2018). In this framework, the joint signals correspond to the same subspace and are orthogonal to individual signals, whereas the individual signals do not intersect (albeit may not be orthogonal). Conceptually, it is clear that (1) separation of joint and individual signals becomes difficult when the angle between individual subspaces gets small; (2) the total rank of the signal must be small to avoid noisy directions being mistaken for the joint due to random overlaps. However, the precise quantification of these concepts has been lacking.

1.1. Our contributions. Our main contribution is an explicit characterization of conditions under which the joint and individual signals are identifiable, which depend on the signal rank, noise level, and principal angles between individual subspaces. Our primary insight is that the spectrum perturbations of the *product of projection matrices*, derived from each view’s estimated subspaces, affect subspace separation. Figure 1 provides a visual illustration of this theoretical result under varying subspace alignment and noise levels. The observed spectrum of the product of projections, which corresponds to the cosine of principal angles between the two subspaces, exhibits a clustering structure that corresponds exactly to joint and individual subspaces. Specifically, the largest singular values close to 1 correspond to joint subspace, the middle singular values correspond to non-orthogonal individual subspaces, and the smallest singular values correspond to orthogonal individual and noise directions. The bars indicate the observed spectrum, whereas the colored areas highlight the theoretically derived predictions on the spectrum perturbation in alignment with observed clustering. A lack of interval overlap supports the idea that joint subspaces are distinguishable from individual subspaces and noise.

Motivated by new theoretical insights on the perturbation of the spectrum of the product of projections, we propose an estimation approach that quantifies these perturbations in practice with an easy-to-use and scalable algorithm. First, we develop a novel rotational bootstrap technique to bound the perturbations of the spectrum corresponding to joint and non-orthogonal individual subspaces (top two clusters). Second, we utilize results from random matrix theory to quantify the maximal alignment possible by chance, providing

a bound on the bottom cluster (orthogonal individual and noisy subspace directions). We use these two bounds to obtain estimates for the joint and individual subspaces. Further, we generate diagnostic plots that visualize cluster partitioning with the two bounds overlaid (like the one in Figure 1), providing practical and interpretable insights regarding the identifiability of joint and individual subspaces.

In simulations, our method is competitive compared to those of Lock et al. (2013); Feng et al. (2018); Gaynanova & Li (2019); Shu et al. (2019); Park & Lock (2020), particularly in terms of true and false discovery rates in estimating joint and individual subspaces. Additionally, we test our approach on colorectal cancer data and nutrigenomic data. The colorectal cancer data includes tumor samples with RNASeq and miRNA views, where we aim to identify joint components. We assess the quality of these components through their predictive power for cancer subtype classification. The nutrigenomic data consists of mice with distinct genotypes and diets, with RNASeq and liver lipid content as the two views. Here, we seek to identify joint and individual components and link them to genotype and diet labels, respectively. In both datasets, our approach achieves the best balance between parsimony and predictive accuracy.

1.2. Related works. Lock et al. (2013); Zhou et al. (2015); Gaynanova & Li (2019); Park & Lock (2020); Yi et al. (2023); Prothero et al. (2024) consider optimization-based approaches for estimating joint and individual subspaces. While effective, these methods can be computationally slow, particularly with high-dimensional data, and often rely on ad-hoc techniques for rank selection (such as permutation or bi-cross-validation). Feng et al. (2018) and Shu et al. (2019) are spectral methods, like ours, and utilize singular value decomposition to derive joint and individual subspaces. Shu et al. (2019) extends canonical correlation analysis to account for individual components. However, the individual components are restricted to be orthogonal, leading to a different model from ours. Feng et al. (2018) uses the spectrum of the average of projection matrices, which contains information about the principle angles between the two subspace views, to estimate joint and individual components. The method allows for non-orthogonal individual signals and is most similar to ours; however, it has certain limitations in comparison, as we discuss below.

Conceptually, Feng et al. (2018) considers the average of projection matrices, while our method is the first to focus on the product of projection matrices. A key disadvantage of using the average of projection matrices is that its spectrum exhibits a provably smaller gap (by a factor of less than one-half in noiseless settings) between individual and joint components than the product. This results in a substantially worse clustering of singular values in practice, especially in moderate to low signal-to-noise regimes (see e.g, Figure 4 in Appendix A.4). The lack of clustering in the spectrum considered by Feng et al. (2018) makes separating the joint directions from the remaining signals more challenging. See § 4 for more numerical comparison and Appendix A.4 for more technical details.

2. MODEL

2.1. Notation. For $a, b \in \mathbb{R}$, let $a \wedge b = \min(a, b)$, $a \vee b = \max(a, b)$. For a matrix $A \in \mathbb{R}^{n \times p}$, write the compact singular value decomposition (SVD) as $A = U\Sigma V^T$, where $\Sigma = \text{diag}(\sigma_1(A), \sigma_2(A), \dots)$ with the singular values $\sigma_1(A) \geq \sigma_2(A) \geq \dots > 0$ in descending order. We denote $\sigma_{\min}(A) = \sigma_{\text{rank}(A)}(A)$, $\sigma_{\max}(A) = \sigma_1(A)$ as the smallest and largest non-trivial singular values. We denote $\sigma(A)$ to be the collection $\{\sigma_1(A), \sigma_2(A), \dots, \sigma_{\text{rank}(A)}(A)\}$. We use $\|A\|_2 = \sigma_1(A)$ to denote the spectral norm, $\|A\|_F$ to denote the Frobenius norm and $\text{col}(A)$ to denote the column space of A . We write the subspaces in calligraphic, e.g., we say $\mathcal{A} \subset \mathbb{R}^n$ to denote a subspace of \mathbb{R}^n . For the projection onto a subspace \mathcal{A} , we write $P_{\mathcal{A}} \in \mathbb{R}^{n \times n}$. For the projection onto the column space of A , we use $P_{\text{col}(A)}$, which can be defined as $P_{\mathcal{A}} = UU^T$. We denote the direct sum of two subspaces \mathcal{A} and \mathcal{B} by $\mathcal{A} \oplus \mathcal{B}$. We adopt the convention to denote the submatrix: $A_{[a:b, c:d]}$ represents the a -to- b -th row, c -to- d -th column of matrix A ; we also use $A_{[a:b, :]}$ and $A_{[:, c:d]}$ to represent a -to- b -th full rows of A and c -to- d -th full columns of A , respectively.

2.2. Setup. Let $Y_1 \in \mathbb{R}^{n \times p_1}, Y_2 \in \mathbb{R}^{n \times p_2}$ be observed data matrices corresponding to two views. The rows of both matrices represent common n subjects, and the columns correspond to the different feature sets collected for each view. For example, in the COAD data (see § 5.1), the first view corresponds to the RNASeq features and the second to the miRNA features. In the nutrigenomic study (see § 5.2), the first view corresponds to the gene expressions and the second view corresponds to the lipid content of the liver. We assume that Y_1, Y_2 are noisy observations of true X_1, X_2 , and consider additive structured signal plus

noise decomposition:

$$(1) \quad Y_k = X_k + Z_k = J_k + I_k + Z_k,$$

where the signal X_k is decomposed into joint part across views (J_k) and the view-specific individual part (I_k), and Z_k is the noise matrix with elements identically and independently distributed according to some distribution.

Model (1) is adopted by many existing methods for multi-view data integration (Lock et al., 2013; Feng et al., 2018; Gaynanova & Li, 2019; Shu et al., 2019; Park & Lock, 2020; Yi et al., 2023; Prothero et al., 2024) with some variations in underlying definitions of joint and individual signals. Here we adopt the original definition as in Lock et al. (2013). To facilitate exposition, consider singular value decomposition representation of each part of the signal:

$$(2) \quad X_k = J_k + I_k = U_{\mathcal{J}_k} \Sigma_{\mathcal{J}_k} V_{\mathcal{J}_k}^\top + U_{\mathcal{I}_k} \Sigma_{\mathcal{I}_k} V_{\mathcal{I}_k}^\top.$$

We refer to $U_{\mathcal{J}_k}$ as joint directions and to $U_{\mathcal{I}_k}$ as individual directions. Joint directions are joint due to the equality of corresponding subspaces, that is they correspond to the joint subspace $\mathcal{J} := \text{col}(U_{\mathcal{J}_1}) = \text{col}(U_{\mathcal{J}_2})$. Thus, joint $U_{\mathcal{J}_1}$ can be reconstructed from joint $U_{\mathcal{J}_2}$ by a rotation by some orthogonal matrix. In contrast, individual directions have non-intersecting subspaces $\mathcal{I}_k := \text{col}(U_{\mathcal{I}_k})$, that is $\mathcal{I}_1 \cap \mathcal{I}_2 = \{\mathbf{0}\}$, which emphasizes that they are indeed specific to each view. For identifiability, joint and individual subspaces are assumed to be orthogonal, that is $\mathcal{J} \perp \mathcal{I}_k$.

However, the individual \mathcal{I}_1 and \mathcal{I}_2 are not necessarily orthogonal and can be further decomposed into orthogonal and non-orthogonal parts, leading to a three-part decomposition (joint, non-orthogonal individual, orthogonal individual). We further provide explicit characterization and identifiability conditions of this three-part decomposition of signal column spaces, which is based on Lemma 1 of Feng et al. (2018) and Proposition 4 of Gaynanova & Li (2019).

Lemma 2.1 (Existence and Identifiability). *Given a set of subspaces $\{\text{col}(X_1), \text{col}(X_2)\}$, there is a unique set of subspaces $\{\mathcal{J}, \mathcal{N}_1, \mathcal{N}_2, \mathcal{O}_1, \mathcal{O}_2\}$ such that:*

- (1) $\text{col}(X_k) = \mathcal{J} \oplus \mathcal{N}_k \oplus \mathcal{O}_k$ with individual $\mathcal{I}_k := \mathcal{N}_k \oplus \mathcal{O}_k$;
- (2) $\mathcal{J} \perp \mathcal{I}_k$, $\mathcal{N}_k \perp \mathcal{O}_l$ for $k \neq l$;
- (3) $\mathcal{O}_1 \perp \mathcal{O}_2$;
- (4) $\bigcap \mathcal{N}_k = \{\mathbf{0}\}$ and maximal principle angle between \mathcal{N}_1 and \mathcal{N}_2 is $< \pi/2$.

Here, the individual subspace is given by $\mathcal{I}_k = \mathcal{N}_k \oplus \mathcal{O}_k$, with \mathcal{N}_k corresponding to non-orthogonal part and \mathcal{O}_k to orthogonal part. The three-part decomposition can be viewed from the perspective of ordering the principal angles between subspaces $\text{col}(X_1)$ and $\text{col}(X_2)$ (§ 3.1). Specifically, it can be viewed as aligning the basis of $\text{col}(X_1)$ and $\text{col}(X_2)$ into pairs, from perfectly aligned pairs (zero angles, joint subspace \mathcal{J}) to somewhat aligned pairs (angles strictly between 0 and $\pi/2$, non-orthogonal \mathcal{N}_1 and \mathcal{N}_2) to orthogonal basis that can not be paired ($\pi/2$ angles, orthogonal \mathcal{O}_1 and \mathcal{O}_2).

Our main goal is to distinguish joint subspace from individual based on the noisy observed Y_k . Conceptually, it is clear that (1) separation of joint and individual signals becomes difficult when the angle between individual subspaces gets small, i.e. the angle between \mathcal{N}_1 and \mathcal{N}_2 ; (2) the total rank of the signal must be small to avoid noisy directions being mistaken for the joint signal due to random overlaps. However, the precise quantification of these concepts has been lacking. Next, we illustrate how the spectrum of the product of projection matrices allows us to distinguish joint subspaces from the aligned individual ones and provide theoretical quantification of the spectrum perturbation as a result of noise. We then use these insights to develop an effective and interpretable estimation approach for joint and individual subspaces.

3. OUR METHOD: PRODUCT OF PROJECTIONS DECOMPOSITION

Our theoretical insights, which subsequently motivate the proposed estimation approach, rely crucially on the product of projection matrices associated with each view’s subspace. The spectrum of this product corresponds to the cosines of principal angles between the pair of subspaces (Bjoerck & Golub, 1971). In noiseless cases, this spectrum can be clustered to perfectly separate joint and individual subspaces (§ 3.1). In the presence of noise, this spectrum is perturbed, and in § 3.2, we quantify these perturbations with respect to each cluster, leading to explicit conditions for correct estimation of joint rank and quantification

of corresponding subspace estimation error. As theoretical perturbation bounds depend on unknown quantities, in § 3.3 we estimate these bounds using rotational bootstrap and random matrix theory, leading to a diagnostic plot that visualizes partitioning of the spectrum into clusters and provides insights into the estimation performance. Throughout, we focus on the case of two views, with Appendix A.3 describing the extension to the larger number of views.

3.1. Product of projections in the noiseless setting. Consider the noiseless case with $Z_k = \mathbf{0}_{n \times p_k}$ so that $Y_k = X_k$. Let $X_k = U_k \Sigma_k V_k^\top$ be the compact singular value decomposition of signal X_k . Using Lemma 2.1, we have:

$$P_{\text{col}(X_k)} = U_k U_k^\top = P_{\mathcal{J}} + P_{\mathcal{I}_k} \quad \Rightarrow \quad P_{\text{col}(X_1)} P_{\text{col}(X_2)} = P_{\mathcal{J}} + P_{\mathcal{I}_1} P_{\mathcal{I}_2}.$$

Consider the second term $P_{\mathcal{I}_1} P_{\mathcal{I}_2}$. Let $U_{\mathcal{J}} \in \mathbb{R}^{n \times \dim(\mathcal{J})}$ be the matrix whose columns form orthonormal basis of \mathcal{J} , similarly let $U_{\mathcal{N}_1}, U_{\mathcal{N}_2}, U_{\mathcal{O}_1}, U_{\mathcal{O}_2}$ be the matrices of the orthonormal bases for $\mathcal{N}_1, \mathcal{N}_2, \mathcal{O}_1, \mathcal{O}_2$. Then,

$$P_{\mathcal{I}_1} P_{\mathcal{I}_2} = (P_{\mathcal{N}_1} + P_{\mathcal{O}_1})(P_{\mathcal{N}_2} + P_{\mathcal{O}_2}) = P_{\mathcal{N}_1} P_{\mathcal{N}_2} = U_{\mathcal{N}_1} U_{\mathcal{N}_1}^\top U_{\mathcal{N}_2} = (U_{\mathcal{N}_1} H) \Sigma (K^\top U_{\mathcal{N}_2}^\top).$$

Here, $H \Sigma K^\top$ is the singular value decomposition of $U_{\mathcal{N}_1}^\top U_{\mathcal{N}_2}$; diagonal entries of Σ equal cosines of the non-zero principal angles between \mathcal{I}_1 and \mathcal{I}_2 . Since $\mathcal{I}_1 \cap \mathcal{I}_2 = \{\mathbf{0}\}$, $\sigma_{\max}(\Sigma) < 1$. Thus,

$$P_{\text{col}(X_1)} P_{\text{col}(X_2)} = [U_{\mathcal{J}} \quad U_{\mathcal{N}_1} H] \begin{bmatrix} I^{\dim \mathcal{J}} & 0 \\ 0 & \Sigma \end{bmatrix} [U_{\mathcal{J}} \quad U_{\mathcal{N}_2} K]^\top,$$

where the matrices $[U_{\mathcal{J}} \quad U_{\mathcal{N}_1} H]$ and $[U_{\mathcal{J}} \quad U_{\mathcal{N}_2} K]$ are orthonormal. Thus, the spectrum of $P_{\text{col}(X_1)} P_{\text{col}(X_2)}$ clusters into two components: a cluster with singular values equal to one and a cluster with singular values in the range $[\sigma_{\min}(\Sigma), \sigma_{\max}(\Sigma)]$. Let r_{clust1} be the number of singular values in the first cluster (corresponding to singular values one). Then, the joint and individual subspaces can be exactly identified via:

$$\begin{aligned} \mathcal{J} &= \text{span of the first } r_{\text{clust1}} \text{ left (or right) singular vectors of } P_{\text{col}(X_1)} P_{\text{col}(X_2)}, \\ \mathcal{I}_k &= \text{span of the first } \text{rank}(X_k) - r_{\text{clust1}} \text{ left (or right) singular vectors of } P_{\text{col}(X_k)}(I - P_{\mathcal{J}}). \end{aligned}$$

Thus, in the noiseless setting, the spectrum of the product of projections $P_{\text{col}(X_1)} P_{\text{col}(X_2)}$ (equivalently, the set of cosines of principle angles between $\text{col}(X_1)$ and $\text{col}(X_2)$) can be divided into two groups. The first group contains values equal to one (equivalently, principle angles 0), whose corresponding singular vectors form a basis for the joint subspace. The second group contains values strictly less than one (equivalently, principle angles strictly greater than 0), reflecting the degree of alignment between the individual subspaces \mathcal{I}_1 and \mathcal{I}_2 . The gap between these two groups, formally defined as one minus the cosine of the smallest principle angle between \mathcal{I}_1 and \mathcal{I}_2 , narrows as the alignment between individual subspaces increases.

3.2. Product of projection matrices in a noisy setting. In practice, we do not have direct access to the subspace $\text{col}(X_k)$ because the signal X_k is unknown. Instead, we have to estimate \widehat{X}_k from noisy observations, with a truncated singular value decomposition of Y_k being a common approach (Feng et al., 2018; Shu et al., 2019). However, the spectrum of the estimated product $P_{\text{col}(\widehat{X}_1)} P_{\text{col}(\widehat{X}_2)}$ differs from the spectrum of the true product $P_{\text{col}(X_1)} P_{\text{col}(X_2)}$ in several key ways. First, even when a joint signal is present, the largest singular values in the estimated product are generally below one and decrease further as the noise level or the dimension of the individual views increases. Second, in the estimated product, the gap between the singular values corresponding to the joint subspaces and those corresponding to the aligned individual subspaces is typically smaller than in the true product. This gap also decreases as noise or dimensionality increases, making it harder to separate joint signals from individual ones, especially when the individual signals are closely aligned. Finally, even when the individual signals are orthogonal, the estimated product may still have small but non-zero singular values, with their magnitudes increasing as the noise level rises.

Our main theoretical contribution lies in the precise characterization of perturbations in the spectrum of $\widehat{M} := P_{\text{col}(\widehat{X}_1)} P_{\text{col}(\widehat{X}_2)}$. Our result provides general guarantees that hold regardless of the estimation procedure used to approximate the signals $(\widehat{X}_1, \widehat{X}_2)$. The quality of the chosen estimation procedure is reflected in our analysis via deterministic quantities $\varepsilon_1 := \|P_{\text{col}(X_1)} (\Delta_1 + \Delta_2 + \Delta_1 \Delta_2) P_{\text{col}(X_2)}\|_2$ and $\varepsilon_2 := \|P_{\text{col}(X_1)} \Delta_2 + \Delta_1 P_{\text{col}(X_2)} + \Delta_1 \Delta_2\|_2$ with $\Delta_k := P_{\text{col}(X_k)} - P_{\text{col}(\widehat{X}_k)}$. The proof is in the Appendix A.1.

Theorem 3.1 (Spectrum of the product of projections). *Let $\tau_{\min} := \sigma_{\min}(P_{\mathcal{N}_1}P_{\mathcal{N}_2})$ and $\tau_{\max} := \sigma_{\max}(P_{\mathcal{N}_1}P_{\mathcal{N}_2})$. If $\text{rank}(X_1), \text{rank}(X_2) > 0$, then the spectrum of \widehat{M} consists of:*

- (1) *a group of $\dim(\mathcal{J})$ singular values in $[1 - \varepsilon_1 \vee 0, 1]$;*
- (2) *a group of $\text{rank}(P_{\mathcal{N}_1}P_{\mathcal{N}_2})$ singular values in $[(\tau_{\min} - \varepsilon_1) \vee 0, (\tau_{\max} + \varepsilon_2) \wedge 1]$;*
- (3) *a remaining group of singular values in $[0, \varepsilon_2 \wedge 1]$.*

This theorem states that in the presence of a signal, the spectrum of the product of projection matrices \widehat{M} organizes into three groups: joint, non-orthogonal individual, and noise directions. The constraint $\varepsilon_1 < \max\{1 - \varepsilon_2, 1 - \sigma_{\max}(P_{\mathcal{N}_1}P_{\mathcal{N}_2}) - \varepsilon_2\}$ ensures that the singular values corresponding to the joint structure are distinguishable from other clusters, that is the number of singular values above $1 - \varepsilon_1$ correctly identifies the joint rank. Similarly, the constraint $\varepsilon_1 + \varepsilon_2 < \sigma_{\min}(P_{\mathcal{N}_1}P_{\mathcal{N}_2})$ ensures that the group of singular values corresponding to the non-orthogonal individual structure is distinguishable from the noise group. When both constraints hold, the spectrum of \widehat{M} has *three non-overlapping clusters* corresponding to joint, non-orthogonal individual, and noise directions. The gap between the clusters decreases with larger values of $\varepsilon_1, \varepsilon_2$ and larger alignment of the non-orthogonal individual subspaces \mathcal{N}_1 and \mathcal{N}_2 . Figure 1 illustrates these theoretical intervals alongside observed singular values of \widehat{M} and true singular values of $P_{\text{col}(X_1)}P_{\text{col}(X_2)}$.

The error terms $\varepsilon_1, \varepsilon_2$ depend on the noise level: higher noise leads to larger perturbations Δ_k in estimating each view, and thus larger values of $\varepsilon_1, \varepsilon_2$. Figure 1 shows how a smaller signal-to-noise ratio results in smaller cluster gaps. The estimated subspace dimension $\text{col}(\widehat{X}_k)$ also affects the size of $\varepsilon_1, \varepsilon_2$. Underestimating the rank (e.g., $\text{rank}(\widehat{X}_1) < \text{rank}(X_1)$) can lead to large ε_1 and ε_2 , especially if missing directions are aligned with both $\text{col}(X_1)$ and $\text{col}(X_2)$. In fact, $\varepsilon_1 = 1$ when a missing direction is part of the joint structure, in which cases the effective number of large singular values corresponding to the joint structure gets smaller than the true joint rank. Overestimating the rank (e.g., $\text{rank}(\widehat{X}_1) > \text{rank}(X_1)$) can also lead to large errors due to increased dimensionality of Δ_k , making the third component of ε_2 , $\|\Delta_1\Delta_2\|_2$, very large, albeit slight overestimation would still keep those terms small. Thus, overestimation is generally preferred to underestimation. We use these insights in § 3.3, providing practical guidelines on marginal rank estimation.

The clustering of the singular values of \widehat{M} enables a natural estimator for the signal subspaces. The joint subspace dimension is estimated as the number of singular values of \widehat{M} above $1 - \varepsilon_1$, denoted by $\widehat{r}_{\mathcal{J}}$. According to Theorem 3.1, this estimate is exact if $\varepsilon_1 < \max\{1 - \varepsilon_2, 1 - \sigma_{\max}(P_{\mathcal{N}_1}P_{\mathcal{N}_2}) - \varepsilon_2\}$. To estimate the joint subspace itself, a candidate approach is to use the span of the first $\widehat{r}_{\mathcal{J}}$ left (or right) singular vectors of \widehat{M} . However, this approach arbitrarily favors one view over the other, insisting that the joint subspace is strictly contained in $\text{col}(\widehat{X}_1)$. To avoid this, we symmetrize the product of projection matrices by $\widehat{S} := \frac{1}{2}(\widehat{M} + \widehat{M}^\top)$, which effectively averages the estimated joint directions from each view, yielding a more accurate estimate. We estimate the joint and individual subspace structures as

$$(3) \quad \begin{aligned} \widehat{\mathcal{J}} &:= \text{span of the first } \widehat{r}_{\mathcal{J}} \text{ singular vectors of } \widehat{S} = \frac{1}{2} \left(P_{\text{col}(\widehat{X}_1)}P_{\text{col}(\widehat{X}_2)} + P_{\text{col}(\widehat{X}_2)}P_{\text{col}(\widehat{X}_1)} \right), \\ \widehat{\mathcal{I}}_k &:= \text{span of the first } \text{rank}(\widehat{X}_k) - \widehat{r}_{\mathcal{J}} \text{ left singular vectors of } P_{\text{col}(\widehat{X}_k)}(I - P_{\widehat{\mathcal{J}}}), \end{aligned}$$

and the following theorem characterizes their quality with the proof in Appendix A.1.

Theorem 3.2 (Estimation Error of the Joint and Individual Subspaces). *Define $R_{\mathcal{J}} := P_{\text{col}(X_1)}\Delta_2 + \Delta_1P_{\text{col}(X_2)} + \Delta_1\Delta_2$ and $R_{\mathcal{I}_k} := P_{\mathcal{J}}\Delta_k + \Delta_{\mathcal{J}}P_{\text{col}(X_k)} + \Delta_{\mathcal{J}}\Delta_k$, where $\Delta_{\mathcal{J}} := P_{\widehat{\mathcal{J}}} - P_{\mathcal{J}}$ and $\Delta_k := P_{\text{col}(X_k)} - P_{\text{col}(\widehat{X}_k)}$. Suppose $\varepsilon_1 < \max\{1 - \varepsilon_2, 1 - \sigma_{\max}(P_{\mathcal{N}_1}P_{\mathcal{N}_2}) - \varepsilon_2\}$. Then,*

$$\dim(\widehat{\mathcal{J}}) = \dim(\mathcal{J}) \quad \text{and} \quad \|P_{\widehat{\mathcal{J}}} - P_{\mathcal{J}}\|_2 \leq \frac{\dim(\mathcal{J})^{1/2} \|R_{\mathcal{J}} + R_{\mathcal{J}}^\top\|_2}{1 - \sigma_{\max}(P_{\mathcal{N}_1}P_{\mathcal{N}_2})}.$$

Further, if the rank of each subspace view is correctly estimated, i.e. $\text{rank}(\widehat{X}_k) = \text{rank}(X_k)$,

$$\|P_{\widehat{\mathcal{I}}_k} - P_{\mathcal{I}_k}\|_2 \leq 2 \dim(\mathcal{I}_k)^{1/2} \|R_{\mathcal{I}_k}\|_2.$$

This theorem quantifies the accuracy of estimated subspaces when the ranks are correctly specified. Since the spectral norm of the difference between two projection matrices equals the sine of the largest principle between the corresponding subspaces, our bounds measure the sine of the largest principle angles between $\widehat{\mathcal{J}}$ and \mathcal{J} , and between $\widehat{\mathcal{I}}_k$ and \mathcal{I}_k , respectively. For joint subspace estimation, the bound depends on the

perturbation term $R_{\mathcal{J}}$ and the maximum alignment $\sigma_{\max}(P_{\mathcal{N}_1}P_{\mathcal{N}_2})$ between the individual subspaces. As in Theorem 3.1, large perturbations and subspace alignment can lead to significant errors, even with the correct rank.

3.3. Practical considerations and proposed algorithm. In practice, our primary goal is to use the observed spectrum of $P_{\text{col}(\widehat{X}_1)}P_{\text{col}(\widehat{X}_2)}$ to accurately determine the joint rank. Our new theoretical insights characterize spectrum perturbation in terms of ε_1 and ε_2 , both of which are unknown in practice. Furthermore, the magnitudes of $\varepsilon_1, \varepsilon_2$ depend on the quality of estimates \widehat{X}_k . Therefore, we focus on the following practical questions: (i) how can we obtain estimates of $\text{col}(\widehat{X}_k)$ for the signal X_k in each view $k \in \{1, 2\}$ to minimize the magnitude of these perturbations? (ii) how can we estimate ε_1 in practice to identify the top cluster of potential joint directions? (iii) how can we bound ε_2 to ensure the top cluster contains only joint directions and avoid overlap from random noise alignment? Below, we outline answers to these practical questions and summarize our proposed method.

(i) Estimation of $\text{col}(X_k)$. To estimate the signal X_k , we construct \widehat{X}_k using truncated singular value decomposition of observed Y_k for each view $k \in \{1, 2\}$. We choose the level of truncation based on the criterion in Gavish & Donoho (2014). Let $\beta_k = n/p_k$ be the aspect ratio, and y_{med} be the median singular value of Y_k . Then we only keep those singular vectors whose corresponding singular values exceed the threshold $(0.56\beta_k^3 - 0.95\beta_k^2 + 1.82\beta_k + 1.43)\widehat{\sigma}_k$. This threshold is designed to obtain an optimal (in mean squared error) reconstruction of the signal matrix. However, it tends to overestimate the true signal rank. As we discuss after Theorem 3.1, overestimating the rank of each view is preferred over underestimation. However, severe overestimation can result in high alignment between random noisy directions, leading to cluster overlap. We will revisit this point in part (iii) and the diagnostic plot generated at the end of the algorithm.

(ii) Estimation of ε_1 via rotational bootstrap. From Theorem 3.1, the number of singular values of \widehat{M} above $1 - \varepsilon_1$ can be used as an estimate of the joint subspace rank. To estimate ε_1 , we propose a novel bootstrap procedure. We first review a rotational bootstrap approach in Prothero et al. (2024) and then describe our proposal.

Prothero et al. (2024) adopt model (1), and estimate the maximal principle angle between the true subspace $\text{col}(X_k)$ and the subspace formed by truncated singular value decomposition of observed Y_k , $\widehat{X}_k = \widehat{U}_k\widehat{\Sigma}_k\widehat{V}_k^\top$, $k \in \{1, 2\}$, with $\widehat{r}_k := \text{rank}(\widehat{X}_k)$. For each bootstrap sample, the data replicate is generated as $Y_{k,(b)} := U_{k,(b)}\widehat{\Sigma}_kV_{k,(b)}^\top + \widehat{E}_k$, where $\widehat{\Sigma}_k$ is a matrix of singular values from \widehat{X}_k , $U_{k,(b)} \in \mathbb{R}^{n \times \widehat{r}_k}$, $V_{k,(b)} \in \mathbb{R}^{p \times \widehat{r}_k}$ are orthonormal, drawn uniformly and independently from the Haar measure, and \widehat{E}_k is the adjusted estimate of the noise matrix (see Appendix C in Prothero et al. (2024)). Here $X_{k,(b)} = U_{k,(b)}\widehat{\Sigma}_kV_{k,(b)}^\top$ represents the signal replicate. Using data replicate $Y_{k,(b)}$, the corresponding truncated singular value decomposition of rank \widehat{r}_k is given by $\widehat{X}_{k,(b)} := \widehat{U}_{k,(b)}\widehat{D}_{(b)}\widehat{V}_{k,(b)}^\top$. The resulting projection matrices $P_{\text{col}(X_k),(b)} := U_{k,(b)}U_{k,(b)}^\top$ and $P_{\text{col}(\widehat{X}_k),(b)} := \widehat{U}_{k,(b)}\widehat{U}_{k,(b)}^\top$ represent one bootstrap sample of the true and estimated signal subspaces, respectively, allowing estimation of principal angles over replications.

In principle, the above procedure could be applied to estimate ε_1 . However, it leads to underestimation of the true value, especially when the estimated ranks are small relative to the ambient dimension, as randomly sampled subspaces are likely to be nearly orthogonal; see Appendix B.2 for numerical demonstrations. This underestimation is because the procedure in Prothero et al. (2024) is performed separately for each view k . Thus, the alignment across views is not preserved.

The main novelty of the proposed bootstrap procedure lies in preserving the spectrum of the product of projections $P_{\text{col}(\widehat{X}_1)}P_{\text{col}(\widehat{X}_2)}$ in each bootstrap replicate, in addition to preserving the individual spectrum of \widehat{X}_k . Specifically, when generating bootstrap samples for each view, we preserve the alignment between the two subspaces rather than sampling uniformly at random. Let $\Sigma_{\widehat{M}}$ be a diagonal matrix containing singular values of $\widehat{M} = P_{\text{col}(\widehat{X}_1)}P_{\text{col}(\widehat{X}_2)}$. To generate $U_{1,(b)}$ and $U_{2,(b)}$ randomly but with pre-specified alignment, we first generate an $n \times n$ matrix N with entries drawn independently from a standard normal distribution. We let $U_{1,(b)}$ consist of the first \widehat{r}_1 left singular vectors of N and $U_{2,(b)}$ consist of the next \widehat{r}_2 left singular vectors. We then align these matrices by updating $U_{2,(b)}$ to be $U_{1,(b)} \cos(\Sigma_{\widehat{M}}) + U_{2,(b)} \sin(\Sigma_{\widehat{M}})$. By construction, the singular values of $U_{1,(b)}^\top U_{2,(b)}$ are exactly $\cos(\Sigma_{\widehat{M}})$. We then proceed as in Prothero et al. (2024), leading

to projection matrices $P_{\text{col}(X_k),(b)} := U_{k,(b)}U_{k,(b)}^\top$ and $P_{\text{col}(\widehat{X}_k),(b)} := \widehat{U}_{k,(b)}\widehat{U}_{k,(b)}^\top$, $k = 1, 2$, for each replicate. Given B bootstrap replicates, we estimate ε_1 as:

$$(4) \quad \widehat{\varepsilon}_1 := \frac{1}{B} \sum_{b=1}^B \|P_{\text{col}(X_1),(b)}(\Delta_{1,(b)} + \Delta_{2,(b)} + \Delta_{1,(b)}\Delta_{2,(b)})P_{\text{col}(X_2),(b)}\|_2,$$

where $\Delta_{k,(b)} = P_{\text{col}(X_k),(b)} - P_{\text{col}(\widehat{X}_k),(b)}$, $k \in \{1, 2\}$. In Appendix B.3, we show numerically that $\widehat{\varepsilon}_1$ tends to overestimate ε_1 and becomes more accurate with a larger signal-to-noise ratio.

(iii) Filtering out noise directions via bound on ε_2 . Due to a low signal-to-noise ratio or rank over-specification, the estimated subspaces $\text{col}(\widehat{X}_1), \text{col}(\widehat{X}_2)$ can include many noise directions. These noise directions can exhibit alignment across the two views by random chance, with the degree of alignment increasing as the number of noise directions grows (due to decreasing signal-to-noise ratio and/or increasing rank over-specification). Such random alignments are reflected by the third cluster of singular values in Theorem 3.1. As ε_2 becomes large, this noise cluster will overlap with the top cluster corresponding to joint directions, preventing accurate identification of the joint signal. To diagnose such cases in practice, we could adapt a similar bootstrap estimation idea to ε_2 as we did to ε_1 in (ii). However, we found that a simpler analytical bound can be obtained by utilizing results from random matrix theory.

To motivate the analytical bound, consider a simplified scenario with no individual signals, $P_{\text{col}(X_k)} = P_{\mathcal{J}}$, with $P_{\text{col}(\widehat{X}_k)} = P_{\mathcal{J}} + P_{\text{noise}_k}$, that is the estimated signal is exactly the joint signal plus orthogonal noise directions. Then $\varepsilon_2 = \|P_{\text{col}(X_1)}\Delta_2 + \Delta_1 P_{\text{col}(X_2)} + \Delta_1\Delta_2\|_2 = \|P_{\text{noise}_1}P_{\text{noise}_2}\|_2$, representing the maximal singular value of the product of random projections. While ε_2 is generally more complex, the key intuition remains: only singular values above the threshold expected from random noise alignment can be confidently identified as the signal.

We explicitly characterize the distribution of the entire spectrum of the product of random projections $P_{\text{noise}_1}P_{\text{noise}_2}$ by leveraging results from random matrix theory, which leads to the proposed analytical bound on $\|P_{\text{noise}_1}P_{\text{noise}_2}\|_2$. Let P_{noise_1} and P_{noise_2} denote two independent projection matrices onto random subspaces (drawn from a Haar measure) of \mathbb{R}^n with ranks r_1 and r_2 . Let $q_k := r_k/n$ for $k \in \{1, 2\}$ be the aspect ratio. Then the asymptotic distribution of λ , the squares of the singular values of $P_{\text{noise}_1}P_{\text{noise}_2}$, as $n \rightarrow \infty$ (Bouchaud et al., 2007) has a continuous part

$$(5) \quad f(\lambda) = \frac{\sqrt{(\lambda_+ - \lambda)(\lambda - \lambda_-)}}{2\pi\lambda(1 - \lambda)}, \quad \lambda_{\pm} = q_1 + q_2 - 2q_1q_2 \pm 2\sqrt{q_1q_2(1 - q_1)(1 - q_2)},$$

and two delta peaks $A_0\delta(\lambda)$ and $A_1\delta(\lambda - 1)$ with $A_0 = 1 - q_1 \wedge q_2$ and $A_1 = (q_1 + q_2 - 1) \vee 0$. We illustrate this distribution in Appendix B.4 as a function of q_1, q_2 . As the number of noisy directions increases, so does the maximal singular value $\|P_{\text{noise}_1}P_{\text{noise}_2}\|_2$, reaching the value of one at $q_1 = q_2 = 1/2$. When $q_1, q_2 < 1/2$, the maximal singular value is given by $\lambda_+^{1/2}$ in (5).

To filter out the noise directions when determining the joint rank, we propose considering only singular values with squares exceeding $\lambda_+^{1/2}$. Since, in practice, the true joint rank is unknown, we use marginal rank(\widehat{X}_k) in place of r_k to determine the aspect ratios q_k in calculating λ_+ . This approach can be viewed as conservative, as it effectively assumes that all the directions in estimated $\text{col}(\widehat{X}_1), \text{col}(\widehat{X}_2)$ are potentially noisy. Further, we illustrate how these bounds can be used to diagnose model performance in practice.

Full algorithm description and diagnostics. In summary, given the observed data matrices (Y_1, Y_2) , we obtain estimates of $\text{col}(\widehat{X}_1)$ and $\text{col}(\widehat{X}_2)$ as in (i) to construct $\widehat{M} = P_{\text{col}(\widehat{X}_1)}P_{\text{col}(\widehat{X}_2)}$. We estimate the rank of the joint subspace $\widehat{r}_{\mathcal{J}}$ as the number of singular values in the spectrum of \widehat{M} that are above $1 - \widehat{\varepsilon}_1 \vee \lambda_+^{1/2}$ where $\widehat{\varepsilon}_1$ and λ_+ are given by (4) and (5), respectively. We estimate the joint and individual subspaces according to (3). We summarize the steps in Appendix A.2.

We accompany our algorithm with a diagnostic plot (e.g., Figure 2 for COAD dataset), which illustrates the spectrum of the product \widehat{M} together with the bounds $1 - \widehat{\varepsilon}_1$ and $\lambda_+^{1/2}$. The best case scenario is observing three clear clusters in the spectrum (see e.g., Figure 1 case of Angle = 50, SNR = 22), which provides distinct separation of joint, non-orthogonal individual, and noise irrespective of threshold estimation. More commonly, we expect to only see two clusters (noise and individual/joint). If the cluster of top values is strictly above the threshold, we can be confident those are joint. In case the cluster is in the middle of the threshold, it likely contains a combination of joint and individual. A lack of clustering structure would imply

a large magnitude of noise, preventing accurate separation. In the latter case, driven by our understanding of the magnitude of $\|P_{\text{noise}_1}, P_{\text{noise}_2}\|_2$ from Appendix B.4, we suggest further decreasing the initial marginal rank estimates to reduce aspect ratios q_1, q_2 , which subsequently reduce λ_+ . In § 5, we illustrate these ideas when analyzing real data.

4. SIMULATIONS ON SYNTHETIC DATA

We use simulated data to evaluate the performance of our proposed product of projections decomposition method for joint and individual structure identification. For comparison, we consider methods of Lock et al. (2013), Feng et al. (2018), Gaynanova & Li (2019), Shu et al. (2019) and Park & Lock (2020).

We simulate data from the model (1) with $Y_k = J_k + I_k + Z_k$, $k = 1, 2$, and $X_k = J_k + I_k$, all representing $n \times p_k$ matrices. We let $n = 50$, $p_1 = 80$, $p_2 = 100$, $\text{rank}(J_k) = 4$, $\text{rank}(I_1) = 5$, and $\text{rank}(I_2) = 4$. We sample the singular values of J_k and I_k independently and identically from the uniform distribution. We sample the row space of J_k and I_k uniformly at random according to the Haar measure. To obtain the column spaces of J_k and I_k , we first generate an $n \times n$ matrix N where each entry is sampled independently from a normal distribution and let UDV^T be the corresponding singular value decomposition; we then set the column space of J_k to be $\text{col}(U_{[:,1:4]})$ and the column space of I_1 to be $\text{col}(U_{[:,5:9]})$; we then generate the column space of I_2 to be $\text{col}(\cos(\phi)U_{[:,5:9]} + \sin(\phi)U_{[:,10:14]})$, where ϕ encodes the largest principle angle between the individual subspaces $\text{col}(I_1)$ and $\text{col}(I_2)$. We sample the entries of the noise matrix $Z_k \in \mathbb{R}^{n \times p_k}$ independently and identically from the Gaussian distribution $\mathcal{N}(0, s_k^2)$. From Theorem 5.32 of Vershynin (2010), the largest singular value of an $n \times p_k$ matrix whose entries are sampled from $\mathcal{N}(0, s^2)$ is bounded by $s(\sqrt{n} + \sqrt{p_k})$. Therefore, to control the signal-to-noise ratio (SNR), we take the noise variance for each view to be $s_k = \|X_k\|_2 / (\text{SNR}(\sqrt{n} + \sqrt{p_k}))$.

The theoretical results of § 3 emphasize three main parameters affecting accurate identification of the subspaces: maximum principle angle between the individual subspaces ϕ , noise level, and the marginal ranks of estimated subspaces. To test the magnitude of each of these effects, we consider $\phi \in \{30^\circ, 90^\circ\}$ and $\text{SNR} \in \{0.5, 2\}$. For the rank estimation, we consider three scenarios: (a) we let each method estimate the ranks based on the default method’s implementation; (b) we supply marginal ranks that are smaller than the truth (under-specified rank); (c) we supply marginal ranks that are larger than the truth (over-specified rank). For (b) and (c), the miss-specification is achieved by sampling uniformly from $\{1, 2, 3\}$ and subtracting it from $\text{rank}(X_k)$ in the under-specified setting or adding it to $\text{rank}(X_k)$ in the over-specified setting, respectively. Since the implementation of Lock et al. (2013), Gaynanova & Li (2019) and Park & Lock (2020) does not allow specification of marginal ranks, we only implement (b) and (c) with methods of Feng et al. (2018), Shu et al. (2019) and our approach.

Choosing the right accuracy measure for unsupervised multi-view decomposition is an open challenge, as discussed in Gaynanova & Sergazinov (2024). Many approaches rely on the percent of variance explained or the marginal view reconstruction. However, the percent of variance explained is maximized by a separate singular value decomposition for each view, favoring a lack of joint structure and larger marginal ranks. On the other hand, signal reconstruction error, though unbiased, does not account for structural assumptions or misclassification of the joint directions as individual signals. We propose a new accuracy measure using the subspace version of the false and true discovery metric from Taeb et al. (2020). For an estimated subspace $\hat{\mathcal{S}}$ of a true subspace \mathcal{S} , we evaluate the true positive proportion (TPP) and false discovery proportion (FDP). These are then combined into a single metric, the F-score:

$$(6) \quad \text{TPP} = \frac{\text{tr}(P_{\hat{\mathcal{S}}}P_{\mathcal{S}})}{\dim(\hat{\mathcal{S}})}, \quad \text{FDP} = \frac{\text{tr}((I - P_{\mathcal{S}})P_{\hat{\mathcal{S}}})}{\dim(\hat{\mathcal{S}})}, \quad \text{F-score} = 2 \cdot \frac{(1 - \text{FDP}) \cdot \text{TPP}}{1 - \text{FDP} + \text{TPP}}.$$

We compute the F-scores for joint and individual subspace estimates and take their average F-score as a final accuracy measure, with larger values indicating better performance.

Table 1 displays mean F-score values across 50 replications for each combination of angle, signal-to-noise ratio, and rank specification. The results align with what is expected based on Theorem 3.1: for each method, the performance deteriorates with larger alignment between individual subspaces (smaller angle), and smaller signal-to-noise ratio. In the large signal-to-noise ratio case, rank under-specification is worse than rank over-specification, which is also in agreement with the theory. In the low signal-to-noise ratio case, the results for default rank estimation are worse than those with controlled rank miss-specification, which we

TABLE 1. Mean F-scores (6) on simulated data, larger values correspond to more accurate estimation of joint and individual subspaces. All values are multiplied by 10. The results are averaged across 50 iterations. The maximum standard error of the mean is 0.03. We highlight the best result in **bold** and underline second best result. We denote by (*) methods that do not allow supplying marginal ranks for each view. We denote Lock et al. (2013) as JIV, Feng et al. (2018) as AJI, Gaynanova & Li (2019) as SLI, Shu et al. (2019) as DCC, Park & Lock (2020) as UNI, and our method as PPD.

	Under-specified rank				Estimated rank				Over-specified rank			
	SNR = 2		SNR=0.5		SNR = 2		SNR=0.5		SNR = 2		SNR=0.5	
	90°	30°	90°	30°	90°	30°	90°	30°	90°	30°	90°	30°
JIV	–	–	–	–	8.27	7.88	4.74	4.33	–	–	–	–
AJI	<u>8.54</u>	<u>7.65</u>	5.07	<u>4.56</u>	<u>9.81</u>	<u>8.55</u>	3.85	3.67	<u>9.17</u>	<u>7.70</u>	<u>5.01</u>	4.70
SLI*	–	–	–	–	9.61	7.84	1.49	1.57	–	–	–	–
DCC	8.61	7.59	<u>5.10</u>	4.52	9.80	8.28	3.78	3.60	9.14	7.53	4.93	4.46
UNI*	–	–	–	–	6.73	6.05	<u>4.34</u>	<u>4.05</u>	–	–	–	–
PPD	8.44	7.86	5.12	4.61	9.91	9.75	3.86	3.67	9.19	8.01	5.07	<u>4.67</u>

suspect is due to significant challenges in estimating rank correctly in this setting, with default estimation likely leading to even larger rank estimation error than controlled miss-specification. In terms of comparison across methods, it is difficult to imagine a uniformly best-performing one since different approaches have different strengths under different scenarios. However, our proposed method achieves the highest accuracy in most settings, followed closely by Feng et al. (2018)’s method. A more detailed empirical and theoretical comparison with Feng et al. (2018) is in Appendix A.4, where we show that our method can more effectively distinguish between joint and individual signals.

5. REAL DATA EXPERIMENTS

5.1. Colorectal cancer data. We analyze colorectal cancer data from the Cancer Genome Atlas with two distinct data views: RNA sequencing (RNAseq) normalized counts and miRNA expression profiles (Guinney et al., 2015). We process the data as in Zhang & Gaynanova (2022), leading to $p_1 = 1572$ RNAseq and $p_2 = 375$ miRNA variables. Colorectal cancer has been classified into four consensus molecular subtypes based on gene expression data (Guinney et al., 2015), and we obtain the labels from the Synapse platform (Synapse ID syn2623706). After filtering for complete data, we arrive at $n = 167$ samples from two views with cancer subtype information. Our goal is to extract joint and individual signals and determine which signals are most predictive for cancer subtypes. We apply the proposed product of projections methods and compare it with other methods from § 4. We also consider standard principal component analysis for each view as the baseline.

First, we determine the ranks corresponding to joint and individual structures for each method. For the proposed approach, we estimate the marginal ranks using the truncation method of Gavish & Donoho (2014). The scree plot for each view is shown in Figure 2 (left), resulting in ranks of 40 and 42, respectively. We then apply the proposed method, generating the diagnostic plot of the observed product of the projections spectrum (Figure 2, middle). In the plot, the blue region represents the noise cutoff $\lambda_+^{1/2}$, and the green region marks the top cluster based on the bootstrap estimate of ε_1 . Observe that the spectrum does not show clear clustering, with the noise directions falling well within the region identified by the bootstrap. This inconsistency is likely due to the high rank-to-dimension ratios, which inflate both bounds and the low signal-to-noise ratio, which affects the bootstrap estimate. To address the inclusion of noise directions, we re-examined the scree plot presented in Figure 2. The initial marginal ranks appeared too high, so we identified the elbow point at rank 16 for each view based on the scree plot.

After adjusting the ranks, we re-applied the proposed approach with the updated diagnostic plot (Figure 2, right). The updated plot shows more distinct clustering, with a clear separation between lower and higher singular values. Both the bootstrap and noise bounds support this observation by identifying the cluster

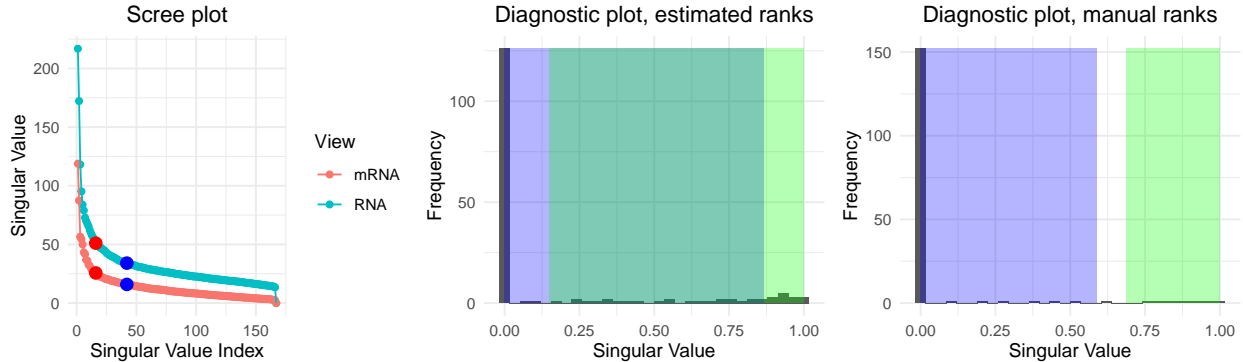


FIGURE 2. **Left:** Scree plot for RNASeq and mRNAseq data. **Blue point** denotes the cutoff suggested by [Gavish & Donoho \(2014\)](#). **Red point** indicates our suggested cutoff. **Middle / Right:** Spectrum of the product of projection matrices onto each view for two different marginal ranks. The **blue region** indicates the random direction bound, $[0, \lambda_+^{1/2}]$, used to filter out the noise directions. The **green region** is given by $[1 - \hat{\varepsilon}_1, 1]$ where $\hat{\varepsilon}_1$ is a bootstrap estimate of ε_1 .

TABLE 2. Mean cancer subtype misclassification rates in percentages together with the minimum principle angle between estimated individual subspaces. We denote principle components analysis by PCA, [Lock et al. \(2013\)](#) as JIV, [Feng et al. \(2018\)](#) as AJI, [Gaynanova & Li \(2019\)](#) as SLI, [Shu et al. \(2019\)](#) as DCC, [Park & Lock \(2020\)](#) as UNI, and our method as PPD.

	Joint (\mathcal{J})		RNAseq (\mathcal{I}_1)		miRNA (\mathcal{I}_2)		Angle $\angle(\mathcal{I}_1, \mathcal{I}_2)$
	Rank	Error	Rank	Error	Rank	Error	
PCA	–	–	16	0	16	6.6	2
JIV	2	44.3	20	0	13	30.5	16
AJI	9	7.2	7	50.9	8	61.7	57
SLI	32	0	41	43.7	10	59.9	90
DCC	9	7.8	7	53.3	7	66.5	90
UNI	1	55.1	5	0	1	44.3	74
PPD	8	8.9	8	53.9	8	62.9	52

of high singular values as the joint structure. This analysis highlights the effectiveness of the proposed diagnostic plot, enabling practitioners to fine-tune parameters to obtain a more confident separation of joint directions.

Next, we evaluate the predictive power of the estimated joint and individual components for cancer subtype classification using multinomial regression. For a fair comparison, we use the same marginal ranks as ours for [Feng et al. \(2018\)](#), [Shu et al. \(2019\)](#), and principal component analysis. For other methods, we use their default rank estimation procedures, as custom ranks could not be specified. We assess classification performance separately for the joint and the individual subspaces. We expect that the joint components will be closely related to the cancer subtype, while the individual components would capture differences between RNA and mRNA platforms unrelated to subtypes. Table 2 shows the estimated ranks, misclassification error rates, and the smallest angle between individual subspaces for each method. As expected, most methods perform better using joint components than individual ones. The exceptions are principal components analysis and the methods of [Lock et al. \(2013\)](#) and [Park & Lock \(2020\)](#). For principle components analysis and [Lock et al. \(2013\)](#), the angles between individual subspaces are small, suggesting that the joint structure may be mistaken for the individual. For [Park & Lock \(2020\)](#), the estimated marginal rank of miRNA view is much smaller compared to all other approaches, so it is possible that the joint structure was

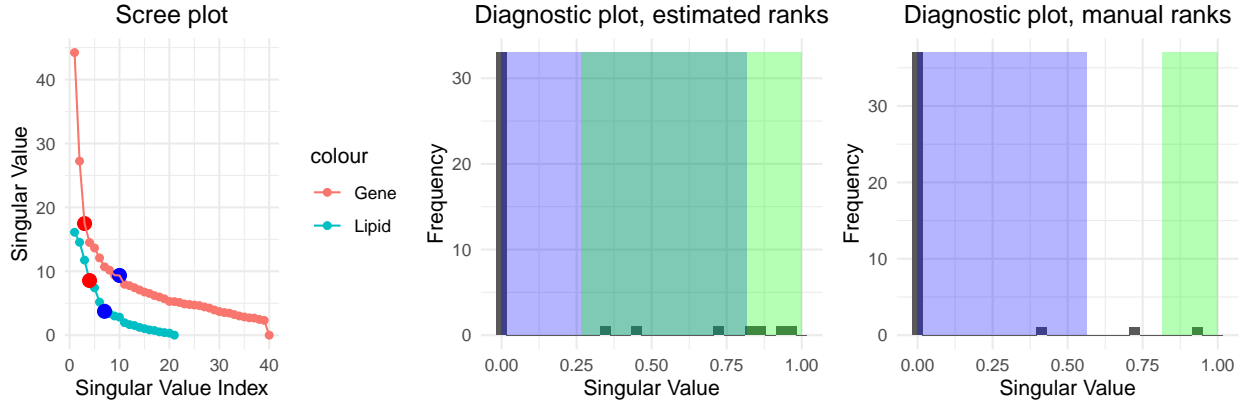


FIGURE 3. **Left:** Scree plot for gene expression and lipid content data. **Blue point** denotes the cutoff suggested by [Gavish & Donoho \(2014\)](#). **Red point** indicates our suggested cutoff. **Middle / Right:** Spectrum of the product of projection matrices onto each view for two different marginal ranks. The **blue region** indicates the random direction bound, $[0, \lambda_+^{1/2}]$, used to filter out the noise directions. The **green region** is given by $[1 - \hat{\varepsilon}_1, 1]$ where $\hat{\varepsilon}_1$ is a bootstrap estimate of ε_1 .

TABLE 3. Mean genotype and diet misclassification rates in percentages together with the minimum principle angle between estimated individual subspaces. We denote principle components analysis by PCA, [Lock et al. \(2013\)](#) as JIV, [Feng et al. \(2018\)](#) as AJI, [Gaynanova & Li \(2019\)](#) as SLI, [Shu et al. \(2019\)](#) as DCC, [Park & Lock \(2020\)](#) as UNI, and our method as PPD.

	Joint (\mathcal{J})			Gene (\mathcal{I}_1)			Lipid (\mathcal{I}_2)			Angles $\angle(\mathcal{I}_1, \mathcal{I}_2)$
	Rank	Type	Diet	Rank	Type	Diet	Rank	Type	Diet	
PCA	–	–	–	3	0	60	4	0	0	22
JIV	2	0	27.5	3	25	57.5	3	30	12.5	44
AJI	2	0	55	1	52.5	77.5	2	47.5	10	66
SLI	6	0	0	8	45	42.5	1	50	57.5	90
DCC	3	0	37.5	1	45	65	1	45	47.5	85
UNI	2	0	62.5	1	52.5	77.5	2	35	0	72
PPD	1	0	80	2	37.5	57.5	3	30	0	44

missed in that view. For joint subspace, [Gaynanova & Li \(2019\)](#) achieves the lowest misclassification rate; however, the corresponding estimated ranks are much higher than for other approaches. In comparison, our method offers a more parsimonious representation of the joint components while retaining strong predictive power, effectively balancing simplicity and informativeness. [Feng et al. \(2018\)](#) and [Shu et al. \(2019\)](#) achieve slightly better miss-classification rates (by 1%) but at the cost of including an additional joint component. From the angles between the individual subspaces reported in Table 2, we see that this additional component corresponds to aligned individual directions with an angle of 52 degrees between the views, which is excluded from the joint subspace in our approach. Indeed, in Figure 2, this angle corresponds to the rotated individual directions by falling exactly in-between our noise bound, $\lambda_+^{1/2}$, and bootstrap bound, $1 - \varepsilon_1$. This again highlights the value of the diagnostic plot and underscores the clear subspace separation achieved by our method.

5.2. Nutrigenomic mice data. The nutrigenomic mice data ([Martin et al., 2007](#)) contain measurements from $n = 40$ mice from two views: gene expressions ($p_1 = 120$) and lipid content of the liver ($p_2 = 21$). The data are available as part of the multi-omics R package ([Rohart et al., 2017](#)). We process the data as

in Yuan et al. (2022). The mice were selected from two genotypes (wild-type and PPAR- α mutant). They were administered five distinct diets consisting of corn and colza oils (ref), a saturated fatty acid diet of hydrogenated coconut oil (coc), an Omega6-rich diet of sunflower oil (sun), an Omega3-rich diet of linseed oil (lin), and a diet with enriched fish oils (fish). Our goal is to identify the joint and individual components across views. We expect that the joint components would be predictive of the mice genotype, while individual components for the lipid view would be predictive of the diet.

As in § 5.1, we start by determining the ranks for each view. The truncation method of Gavish & Donoho (2014) leads to ranks 11 and 7 for gene expressions and lipid concentrations, respectively. Figure 3, left, shows the corresponding scree plot, which suggests that the selected ranks may be too large. Our proposed diagnostic plot based on these ranks is displayed in Figure 3, middle. The noise bound is quite large, and overlaps with the bootstrap bound, suggesting that the rank reduction would be beneficial in filtering the noise directions. Previous analysis of these data has used ranks 3 for genes and 4 for lipids (Yuan et al., 2022). These ranks appear to better align with an elbow on the scree plot and lead to a diagnostic plot with a clear clustering structure and lack of overlap (Figure 3, right). We thus use these ranks for subsequent analysis.

We evaluate the predictive power of the estimated joint and individual components separately for the classification of genotype and diet based on multinomial linear regression. Table 3 shows that the identified joint components for all methods perfectly separate the genotype, with our method providing the most parsimonious representation of rank equal to one. Predicting the diet from the individual lipid features turns out to be a harder task, with only our method and that of Park & Lock (2020) achieving the perfect classification. While principle components analysis also achieves perfect diet classification, the angle between individual components of 22 degrees is small and suggests a missing joint structure. A closer look at Figure 3 shows that the perfect classification of diet by our method is based on the rotated individual direction, which is not part of our joint estimate. In contrast, Feng et al. (2018)’s method treats this direction as a joint component, leading to worse diet classification accuracy. As in the example from Section 5.1, the diagnostic plot proves valuable in evaluating the potential over-specification of ranks and providing confidence in the separation of joint and individual components.

6. CONCLUSION

In this work, we describe a multi-view data decomposition method that naturally derives from the identifiability conditions for joint and individual subspaces. The advantages of our approach include subspace estimation guarantees, scalability, and interpretable diagnostics.

Our work opens several avenues for future research. First, it would be valuable to rigorously extend our method to the multi-view setting with partially shared joint signals. Our current extension in Appendix A.3 assumes fully shared joint components and selects the joint rank via pairwise testing. Second, further theoretical developments could elucidate the properties of our rotational bootstrap approach and refine the asymptotic characterization of the noise bound to account for non-random subspaces. Finally, since many practical applications emphasize predictive performance, extending our method to the semi-supervised setting, as in Park et al. (2021); Palzer et al. (2022), would be beneficial.

7. ACKNOWLEDGEMENTS

Armeen Taeb is supported by NSF DMS-2413074 and by the Royalty Research Fund at the University of Washington. Irina Gaynanova’s research was supported by NSF DMS-2422478.

REFERENCES

- BJOERCK, A. & GOLUB, G. H. (1971). Numerical methods for computing angles between linear subspaces. In *Milestones in Matrix Computation*.
- BOUCHAUD, J.-P., LALOUX, L., MICELI, M. A. & POTTERS, M. (2007). Large dimension forecasting models and random singular value spectra. *The European Physical Journal B* **55**, 201–207.
- FENG, Q., JIANG, M., HANNIG, J. & MARRON, J. (2018). Angle-based joint and individual variation explained. *Journal of multivariate analysis* **166**, 241–265.

- GAVISH, M. & DONOHO, D. L. (2014). The optimal hard threshold for singular values is $4/\sqrt{3}$. *IEEE Transactions on Information Theory* **60**, 5040–5053.
- GAYNANOVA, I. & LI, G. (2019). Structural learning and integrative decomposition of multi-view data. *Biometrics* **75**, 1121–1132.
- GAYNANOVA, I. & SERGAZINOV, R. (2024). Comments on: Data integration via analysis of subspaces (divas). *TEST*, 1–8.
- GUINNEY, J., DIENSTMANN, R., WANG, X., DE REYNIES, A., SCHLICKEK, A., SONESON, C., MARISA, L., ROEPMAN, P., NYAMUNDANDA, G., ANGELINO, P. et al. (2015). The consensus molecular subtypes of colorectal cancer. *Nature medicine* **21**, 1350–1356.
- HOTELLING, H. (1936). Relations between two sets of variates. *Biometrika* **28(3-4)**, 321–377.
- LOCK, E. F., HOADLEY, K. A., MARRON, J. S. & NOBEL, A. B. (2013). Joint and individual variation explained (jive) for integrated analysis of multiple data types. *The annals of applied statistics* **7**, 523.
- MARTIN, P. G., GUILLOU, H., LASSERRE, F., DÉJEAN, S., LAN, A., PASCUSI, J.-M., SANCRISTOBAL, M., LEGRAND, P., BESSE, P. & PINEAU, T. (2007). Novel aspects of ppar α -mediated regulation of lipid and xenobiotic metabolism revealed through a nutrigenomic study. *Hepatology* **45**, 767–777.
- MURDEN, R. J., ZHANG, Z., GUO, Y. & RISK, B. B. (2022). Interpretive jive: Connections with cca and an application to brain connectivity. *Frontiers in Neuroscience* **16**, 969510.
- PALZER, E. F., WENDT, C. H., BOWLER, R. P., HERSH, C. P., SAFO, S. E. & LOCK, E. F. (2022). sjive: Supervised joint and individual variation explained. *Computational statistics & data analysis* **175**, 107547.
- PARK, J. Y. & LOCK, E. F. (2020). Integrative factorization of bidimensionally linked matrices. *Biometrics* **76**, 61–74.
- PARK, S., CEULEMANS, E. & VAN DEUN, K. (2021). Sparse common and distinctive covariates regression. *Journal of Chemometrics* **35**, e3270.
- PROTHERO, J., JIANG, M., HANNIG, J., TRAN-DINH, Q., ACKERMAN, A. & MARRON, J. (2024). Data integration via analysis of subspaces (divas). *TEST*, 1–42.
- ROHART, F., GAUTIER, B., SINGH, A. & LÊ CAO, K.-A. (2017). mixomics: An r package for ‘omics feature selection and multiple data integration. *PLoS computational biology* **13**, e1005752.
- SHU, H., WANG, X. & ZHU, H. (2019). D-cca: A decomposition-based canonical correlation analysis for high-dimensional datasets. *Journal of the American Statistical Association*.
- TAEB, A., SHAH, P. & CHANDRASEKARAN, V. (2020). False discovery and its control in low rank estimation. *Journal of the Royal Statistical Society Series B: Statistical Methodology* **82**, 997–1027.
- VAN DEUN, K., SMILDE, A. K., VAN DER WERF, M. J., KIERS, H. A. & VAN MECHELEN, I. (2009). A structured overview of simultaneous component based data integration. *BMC bioinformatics* **10**, 1–15.
- VERSHYNIN, R. (2010). Introduction to the non-asymptotic analysis of random matrices. *arXiv preprint arXiv:1011.3027*.
- YANG, Z. & MICHAELIDIS, G. (2016). A non-negative matrix factorization method for detecting modules in heterogeneous omics multi-modal data. *Bioinformatics* **32**, 1–8.
- YI, S., WONG, R. K. W. & GAYNANOVA, I. (2023). Hierarchical Nuclear Norm Penalization for Multi-View Data Integration. *Biometrics* **79**, 2933–2946.
- YU, Y., WANG, T. & SAMWORTH, R. J. (2015). A useful variant of the davis–kahan theorem for statisticians. *Biometrika* **102**, 315–323.
- YUAN, D., ZHANG, Y., GUO, S., WANG, W. & GAYNANOVA, I. (2022). Exponential canonical correlation analysis with orthogonal variation. *arXiv preprint arXiv:2208.00048*.
- ZHANG, Y. & GAYNANOVA, I. (2022). Joint association and classification analysis of multi-view data. *Biometrics* **78**, 1614–1625.
- ZHOU, G., CICHOCKI, A., ZHANG, Y. & MANDIC, D. P. (2015). Group component analysis for multiblock data: Common and individual feature extraction. *IEEE transactions on neural networks and learning systems* **27**, 2426–2439.

A.1. Proofs of main results.

Lemma A.1. *Let $X, Y \in \mathbb{R}^{n \times n}$. If $X^\top Y = 0$ or $XY^\top = 0$, then*

- (1) $\sigma_r(X + Y) \geq \max(\sigma_r(X), \sigma_r(Y))$ for all $r \geq 1$ (assuming $\sigma_1 \geq \sigma_2 \geq \dots \geq 0$)
- (2) $\sigma_1^2(X + Y) \leq \sigma_1^2(X) + \sigma_1^2(Y)$

Proof. Without loss of generality, consider $X^\top Y = 0$ (proof is analogous for $XY^\top = 0$). Consider

$$(X + Y)^\top (X + Y) = X^\top X + Y^\top Y.$$

Thus, we have the eigenvalues satisfy

$$\lambda_r\{(X + Y)^\top (X + Y)\} = \lambda_r(X^\top X + Y^\top Y).$$

Weyl's inequality states:

$$\begin{aligned} \lambda_n(Y^\top Y) + \lambda_r(X^\top X) &\leq \lambda_r(X^\top X + Y^\top Y) \leq \lambda_1(Y^\top Y) + \lambda_r(X^\top X) \\ \lambda_n(X^\top X) + \lambda_r(Y^\top Y) &\leq \lambda_r(X^\top X + Y^\top Y) \leq \lambda_1(X^\top X) + \lambda_r(Y^\top Y) \end{aligned}$$

$$\lambda_r(X^\top X + Y^\top Y) \leq \min\{\lambda_r(X^\top X) + \lambda_1(Y^\top Y), \lambda_1(X^\top X) + \lambda_r(Y^\top Y)\}$$

Recall that $\sigma_r^2(A) = \lambda_r(A^\top A)$. Since $\lambda_n(Y^\top Y) \geq 0$, $\lambda_n(X^\top X) \geq 0$, we get (1). Similarly, since $\lambda_1(Y^\top Y) \geq 0$, $\lambda_1(X^\top X) \geq 0$, taking $r = 1$ yields (2). \square

Theorem A.2 (Spectrum of the product of projection matrices). *Let $\widehat{M} := P_{\text{col}(\widehat{X}_1)} P_{\text{col}(\widehat{X}_2)}$. Suppose that $\text{rank}(X_1), \text{rank}(X_2) > 0$. Define*

$$\epsilon_1 := \|P_{\text{col}(X_1)} (\Delta_1 + \Delta_2 + \Delta_1 \Delta_2) P_{\text{col}(X_2)}\|_2, \quad \epsilon_2 := \|P_{\text{col}(X_1)} \Delta_2 + \Delta_1 P_{\text{col}(X_2)} + \Delta_1 \Delta_2\|_2$$

with $\Delta_k := P_{\text{col}(X_k)} - P_{\text{col}(\widehat{X}_k)}$. Then the spectrum of \widehat{M} consists of:

- (1) a group of $\dim(\mathcal{J})$ singular values in $[1 - \epsilon_1 \vee 0, 1]$;
- (2) a group of $\text{rank}(P_{\mathcal{N}_1} P_{\mathcal{N}_2})$ singular values in $[(\sigma_{\min}(P_{\mathcal{N}_1} P_{\mathcal{N}_2}) - \epsilon_1) \vee 0, (\sigma_{\max}(P_{\mathcal{N}_1} P_{\mathcal{N}_2}) + \epsilon_2) \wedge 1]$;
- (3) a remaining group of singular values in $[0, \epsilon_2 \wedge 1]$.

Proof. First, we know from Section 3.1 that

$$(7) \quad P_{\text{col}(X_1)} P_{\text{col}(X_2)} = P_{\mathcal{J}} + P_{\mathcal{I}_1} P_{\mathcal{I}_2} = P_{\mathcal{J}} + P_{\mathcal{N}_1} P_{\mathcal{N}_2} = [U_{\mathcal{J}} \quad U_{\mathcal{N}_1} H] \begin{bmatrix} I_{\dim \mathcal{J}} & 0 \\ 0 & \Sigma \end{bmatrix} [U_{\mathcal{J}} \quad U_{\mathcal{N}_2} K]^\top,$$

where Σ is diagonal corresponding to the cosines of the non-zero principle angles between \mathcal{I}_1 and \mathcal{I}_2 . Thus, $\sigma_r(P_{\text{col}(X_1)} P_{\text{col}(X_2)}) = 1$ for $1 \leq r \leq \dim(\mathcal{J})$ and $\sigma_r(P_{\text{col}(X_1)} P_{\text{col}(X_2)}) = \sigma_{r - \dim(\mathcal{J}) + 1}$ for $\dim(\mathcal{J}) + 1 \leq r \leq \dim(\mathcal{J}) + \text{rank}(P_{\mathcal{I}_1} P_{\mathcal{I}_2})$.

The upper bound for each cluster follows directly from applying Weyl's inequality as

$$\begin{aligned} \sigma_r(\widehat{M}) &= \sigma_r(P_{\text{col}(X_1)} P_{\text{col}(X_2)} + P_{\text{col}(X_1)} \Delta_2 + \Delta_1 P_{\text{col}(X_2)} + \Delta_1 \Delta_2) \\ &\leq \sigma_r(P_{\text{col}(X_1)} P_{\text{col}(X_2)}) + \epsilon_2. \end{aligned}$$

To get the lower bound, we rewrite \widehat{M} as:

$$\begin{aligned} \widehat{M} &= P_{\text{col}(X_1)} P_{\text{col}(X_2)} + P_{\text{col}(X_1)} \Delta_2 + \Delta_1 P_{\text{col}(X_2)} + \Delta_1 \Delta_2 \\ &= \underbrace{P_{\text{col}(X_1)} (I + \Delta_1 + \Delta_2 + \Delta_1 \Delta_2) P_{\text{col}(X_2)}}_{:= A_1} + \underbrace{P_{\text{col}(X_1)} (\Delta_2 + \Delta_1 \Delta_2) (I - P_{\text{col}(X_2)})}_{:= A_2} \\ &\quad + \underbrace{(I - P_{\text{col}(X_1)}) (\Delta_1 + \Delta_1 \Delta_2) P_{\text{col}(X_2)}}_{:= A_3} + \underbrace{(I - P_{\text{col}(X_1)}) \Delta_1 \Delta_2 (I - P_{\text{col}(X_2)})}_{:= A_4} \end{aligned}$$

Note that by construction we have:

- (1) $(A_1 + A_2)^\top (A_3 + A_4) = 0$,
- (2) $A_1 A_2^\top = 0$.

Then it holds that

$$\begin{aligned}
\sigma_r(\widehat{M}) &\geq \sigma_r(A_1 + A_2) && \text{(Lemma A.1)} \\
&\geq \sigma_r(A_1) && \text{(Lemma A.1)} \\
&\geq \sigma_r(P_{\text{col}(X_1)}P_{\text{col}(X_2)}) - \epsilon_1. && \text{(Weyl's inequality)}
\end{aligned}$$

□

Theorem A.3 (Estimation Error). *Suppose $\epsilon_1 < \max\{1 - \epsilon_2, 1 - \sigma_{\max}(P_{\mathcal{N}_1}P_{\mathcal{N}_2}) - \epsilon_2\}$. Define $R_{\mathcal{J}} := P_{\text{col}(X_1)}\Delta_2 + \Delta_1P_{\text{col}(X_2)} + \Delta_1\Delta_2$ and $R_{\mathcal{I}_k} := P_{\mathcal{J}}\Delta_k + \Delta_{\mathcal{J}}P_{\text{col}(X_k)} + \Delta_{\mathcal{J}}\Delta_k$, where $\Delta_{\mathcal{J}} := P_{\widehat{\mathcal{J}}} - P_{\mathcal{J}}$ and $\Delta_k := P_{\text{col}(X_k)} - P_{\text{col}(\widehat{X}_k)}$. Then, $\dim(\widehat{\mathcal{J}}) = \dim(\mathcal{J})$ and the deviation of the estimated joint subspace from the true joint subspace is bounded by*

$$\|P_{\widehat{\mathcal{J}}} - P_{\mathcal{J}}\|_2 \leq \frac{\dim(\mathcal{J})^{1/2} \|R_{\mathcal{J}} + R_{\mathcal{J}}^\top\|_2}{1 - \sigma_{\max}(P_{\mathcal{N}_1}P_{\mathcal{N}_2})}.$$

Furthermore, if the rank of each subspace view is correctly estimated, i.e. $\text{rank}(\widehat{X}_k) = \text{rank}(X_k)$, then, the deviation of the estimated individual subspace from the true individual subspace is bounded by

$$\|P_{\widehat{\mathcal{I}}_k} - P_{\mathcal{I}_k}\|_2 \leq 2 \dim(\mathcal{I}_k)^{1/2} \|R_{\mathcal{I}_k}\|_F.$$

In the proof of Theorem 3.2, we use the adaptation of Davis-Kahan Theorem introduced in Yu et al. (2015). The theorem is stated in terms of the $\sin \Theta$ distance between the subspaces. To apply the theorem, we state the definition of the $\sin \Theta$ distance and principle angles here. Specifically, the $\sin \Theta$ distance is used to measure the difference between two $p \times r$ orthogonal columns \widehat{V} and V . Suppose the singular values of $V^\top \widehat{V}$ are $\sigma_1 \geq \sigma_2 \geq \dots \geq \sigma_r \geq 0$. Then we call

$$\Theta(\widehat{V}, V) = \text{diag}(\cos^{-1}(\sigma_1), \cos^{-1}(\sigma_2), \dots, \cos^{-1}(\sigma_r))$$

as the principle angles. A quantitative measure of distance between the column spaces of \widehat{V} and V is then $\|\sin \Theta(\widehat{V}, V)\|_2$ or $\|\sin \Theta(\widehat{V}, V)\|_F$. Note that the difference of projection matrices, $(P_{\text{col}(\widehat{V})} - P_{\text{col}(V)})$, is related to the $\sin \Theta$ via the equality $\|P_{\text{col}(\widehat{V})} - P_{\text{col}(V)}\|_2 = \|\sin \Theta(\widehat{V}, V)\|_2$

Proof. We treat the joint and individual components separately.

Joint components. To apply Davis-Kahan theorem, we show that there exists an eigengap in the population-level model $S = \frac{1}{2} (P_{\text{col}(X_1)}P_{\text{col}(X_2)} + P_{\text{col}(X_2)}P_{\text{col}(X_1)})$.

From Section 3.1, we know that $S = P_{\mathcal{J}} + \frac{1}{2} (P_{\mathcal{N}_1}P_{\mathcal{N}_2} + P_{\mathcal{N}_2}P_{\mathcal{N}_1})$. Fix an orthonormal basis, $U_{\mathcal{J}}$, for $P_{\mathcal{J}}$. Since $\mathcal{J} \perp \mathcal{N}_k$, we have that $SU_{\mathcal{J}} = U_{\mathcal{J}}$. Hence, S has at least $\dim(\mathcal{J})$ eigenvalues that are equal to 1 with corresponding eigenvectors forming \mathcal{J} . Now fix any orthonormal vector $u \in \text{span}(U_{\mathcal{J}}^\perp)$. Then we have:

$$\begin{aligned}
\|Su\|_2 &= \|P_{\mathcal{J}}u + \frac{1}{2} (P_{\mathcal{N}_1}P_{\mathcal{N}_2} + P_{\mathcal{N}_2}P_{\mathcal{N}_1})u\|_2 \\
&\leq \|P_{\mathcal{N}_1}P_{\mathcal{N}_2}\|_2 && \text{(by triangle-inequality)} \\
&< 1 && \text{(since } \mathcal{I}_1 \cap \mathcal{I}_2 = \{\mathbf{0}\}\text{)}
\end{aligned}$$

Therefore, the spectrum of S becomes $\sigma_r(S) = 1$ for $1 \leq r \leq \dim(\mathcal{J})$ and $\sigma_r(S) \leq \sigma_{\max}(P_{\mathcal{N}_1}P_{\mathcal{N}_2}) < 1$ for $r > \dim(\mathcal{J})$.

From here, applying Davis-Kahan, we have that:

$$\|\sin \Theta(U_{\widehat{\mathcal{J}}}, U_{\mathcal{J}})\|_2 \leq \frac{2 \dim(\mathcal{J})^{1/2} \|\widehat{S} - S\|_2}{1 - \sigma_{\max}(P_{\mathcal{N}_1}P_{\mathcal{N}_2})}$$

Algorithm 1: Algorithmic implementation of our method

Input: Data matrices from two views $Y_1 \in \mathbb{R}^{n \times p_1}$ and $Y_2 \in \mathbb{R}^{n \times p_2}$.

- (1) **Estimate marginal view signals** \widehat{X}_k by truncated singular value decomposition of Y_k with rank as in [Gavish & Donoho \(2014\)](#)
- (2) **Compute perturbation bound** $\widehat{\varepsilon}_1$ by using rotational bootstrap in (4).
- (3) **Compute noise bound** λ_+ based on (5) with $q_k = \text{rank}(\widehat{X}_k)/n$.
- (4) **Estimate joint rank** $\widehat{r}_{\mathcal{J}} = |\{\sigma(\widehat{M}) > \lambda_+^{1/2} \vee (1 - \widehat{\varepsilon}_1)\}|$ with $\widehat{M} = P_{\text{col}(\widehat{X}_1)} P_{\text{col}(\widehat{X}_2)}$
- (5) **Estimate joint subspace** $\widehat{\mathcal{J}}$ as the span of the first $\widehat{r}_{\mathcal{J}}$ singular vectors of $\widehat{S} = (\widehat{M} + \widehat{M}^\top)/2$
- (6) **Estimate individual subspaces** $\widehat{\mathcal{I}}_k$ as span of the first left $\text{rank}(\widehat{X}_k) - \widehat{r}_{\mathcal{J}}$ singular vectors of $P_{\text{col}(\widehat{X}_k)}(I - P_{\widehat{\mathcal{J}}})$.

Output: Joint subspace $\widehat{\mathcal{J}}$ and individual subspaces $\widehat{\mathcal{I}}_1$ and $\widehat{\mathcal{I}}_2$; a histogram of the spectrum of \widehat{M} overlaid with $\lambda_+^{1/2}$, $1 - \widehat{\varepsilon}_1$ and the distribution $f(\lambda)$ in (5).

Putting everything together, we have:

$$\begin{aligned}
 \|P_{\widehat{\mathcal{J}}} - P_{\mathcal{J}}\|_2 &= \|\sin \Theta(U_{\widehat{\mathcal{J}}}, U_{\mathcal{J}})\|_2 \\
 &\leq \frac{2 \dim(\mathcal{J})^{1/2} \|\widehat{S} - S\|_2}{1 - \sigma_{\max}(P_{\mathcal{N}_1} P_{\mathcal{N}_2})} \\
 &\leq \frac{\dim(\mathcal{J})^{1/2} \|P_{\text{col}(X_1)} \Delta_2 + \Delta_1 P_{\text{col}(X_2)} + \Delta_1 \Delta_2 + \Delta_2 P_{\text{col}(X_1)} + P_{\text{col}(X_2)} \Delta_1 + \Delta_2 \Delta_1\|_2}{1 - \sigma_{\max}(P_{\mathcal{N}_1} P_{\mathcal{N}_2})} \\
 &= \frac{\dim(\mathcal{J})^{1/2} \|R_{\mathcal{J}} + R_{\mathcal{J}}^\top\|_2}{1 - \sigma_{\max}(P_{\mathcal{N}_1} P_{\mathcal{N}_2})}.
 \end{aligned}$$

Individual components. Since $\mathcal{J} \perp \mathcal{I}_1$ and $\mathcal{J} \perp \mathcal{I}_2$, we have that $P_{\mathcal{J}^\perp} P_{\text{col}(X_1)} = P_{\mathcal{I}_1}$ and $P_{\mathcal{J}^\perp} P_{\text{col}(X_2)} = P_{\mathcal{I}_2}$. Therefore, we have that $P_{\mathcal{J}^\perp} P_{\text{col}(X_k)}$ has exactly $r_{\mathcal{I}_k}$ eigenvalues equal to 1 and the rest equal to 0. Therefore, applying Davis-Kahan, we get:

$$\begin{aligned}
 \|P_{\widehat{\mathcal{I}}_k} - P_{\mathcal{I}_k}\|_2 &= \|\sin \Theta(U_{\widehat{\mathcal{I}}_k}, U_{\mathcal{I}_k})\|_2 \\
 &\leq 2 \dim(\mathcal{I}_k)^{1/2} \|P_{\mathcal{J}} \Delta_k + \Delta_{\mathcal{J}} P_{\text{col}(X_k)} + \Delta_{\mathcal{J}} \Delta_k\|_2 \\
 &= 2 \dim(\mathcal{I}_k)^{1/2} \|R_{\mathcal{I}_k}\|_2.
 \end{aligned}$$

□

A.2. Algorithm implementation. We provide the full implementation of our method in [Algorithm 1](#). Recall from [Section 3.3](#), given the observed data matrices (Y_1, Y_2) , we first obtain estimates of $\text{col}(\widehat{X}_1)$ and $\text{col}(\widehat{X}_2)$ following [Gavish & Donoho \(2014\)](#). Using these estimates, we construct $\widehat{M} = P_{\text{col}(\widehat{X}_1)} P_{\text{col}(\widehat{X}_2)}$. We then estimate the rank of the joint subspace $\widehat{r}_{\mathcal{J}}$ by counting the number of singular values in the spectrum of \widehat{M} that exceed $(1 - \widehat{\varepsilon}_1) \vee \lambda_+^{1/2}$, where $\widehat{\varepsilon}_1$ and λ_+ are defined in equations (4) and (5), respectively. The joint and individual subspaces are estimated according to equation (3).

A.3. Extension to multi-view case. For the case of $k > 2$, we establish the following lemma on the identifiability, motivated by [Feng et al. \(2018\)](#). The main difference from the previous [Lemma 2.1](#) is that for the multi-view case, we further assume absence of the partially shared structures. That is the joint subspace is a shared between all the view.

Lemma A.4 (Identifiability). *Given a set of subspaces $\{\text{col}(X_1), \dots, \text{col}(X_K)\}$, there is a unique set of subspaces $\{\mathcal{J}, \mathcal{I}_1, \dots, \mathcal{I}_K\}$ such that:*

- (1) $\text{col}(X_k) = \mathcal{J} \oplus \mathcal{I}_k$ with $\mathcal{J} \subseteq \text{col}(X_k)$
- (2) $\mathcal{J} \perp \mathcal{I}_k$
- (3) $\bigcap \mathcal{I}_k = \{\mathbf{0}\}$.

With the above in mind, we propose to identify the joint rank by testing each pair of views separately and setting the joint rank as the the minimum pairwise estimated joint rank. Specifically, we set $\dim \widehat{\mathcal{J}} = \min_{1 \leq i < j \leq k} \dim \widehat{\mathcal{J}}_{ij}$, where $\widehat{\mathcal{J}}_{ij}$ is the joint identified by considering views i and j respectively. To understand why we take the minimum, we consider the following example. Suppose $\dim \widehat{\mathcal{J}}_{12} > \dim \widehat{\mathcal{J}}_{13}$. The directions that have been identified for each pair are above the strict noise bound and the bootstrap bound. This means that we can rule out the possibility that some directions in $\widehat{\mathcal{J}}_{12}$ or $\widehat{\mathcal{J}}_{13}$ are the result of pure noise. This means the estimate $\dim \widehat{\mathcal{J}}_{12}$ includes highly aligned signal directions between the two views. In general, our bootstrap bound always overestimates the true bound for the joint as we highlight in Section B. Therefore, we are confident that this aligned directions in $\widehat{\mathcal{J}}_{12}$ must correspond to the highly rotated individual subspaces, and not the corrupted joint signal. Therefore, by the above logic, we must exclude these directions from our final estimate of the joint.

We estimate the joint subspace by taking the top $\dim \widehat{\mathcal{J}}$ singular vectors of the following symmetric product of projections $\frac{1}{|\mathcal{P}|} \sum_{(i_1, i_2, \dots, i_k) \in \mathcal{P}} P_{\text{col}(\widehat{X}_{i_1})} P_{\text{col}(\widehat{X}_{i_2})} \cdots P_{\text{col}(\widehat{X}_{i_k})}$, where \mathcal{P} is the set of all permutations of $\{1, 2, \dots, k\}$. In Theorem A.5, we show that a similar subspace estimation error bound holds for the multi-view case as in the case of two views.

Theorem A.5 (Estimation Error for $K > 2$). *Suppose our estimate of the joint rank is correct, i.e., $\dim \widehat{\mathcal{J}} = \dim \mathcal{J}$. Define $W_{i_j}(\mathcal{S}) = P_{\text{col}(X_{i_j})} \mathbb{I}[i_j \in \mathcal{S}] + \Delta_{i_j} \mathbb{I}[i_j \notin \mathcal{S}]$ and $R_{\mathcal{I}_k} := P_{\mathcal{J}} \Delta_k + \Delta_{\mathcal{J}} P_{\text{col}(X_k)} + \Delta_{\mathcal{J}} \Delta_k$, where $\Delta_{\mathcal{J}} := P_{\widehat{\mathcal{J}}} - P_{\mathcal{J}}$ and $\Delta_k := P_{\text{col}(X_k)} - P_{\text{col}(\widehat{X}_k)}$. Additionally, let \mathcal{P} be the set of all permutations of $\{1, 2, \dots, K\}$. Then, the deviation of the estimated joint subspace from the true joint subspace is bounded by:*

$$\|P_{\widehat{\mathcal{J}}} - P_{\mathcal{J}}\|_2 \leq \frac{2 \dim(\mathcal{J})^{1/2} \left\| \sum_{\mathcal{S} \subset \{1, 2, \dots, K\}} \prod_{j=1}^K W_{i_j}(\mathcal{S}) \right\|_2}{|\mathcal{P}| \left(1 - \frac{1}{|\mathcal{P}|} \sum_{(i_1, i_2, \dots, i_k) \in \mathcal{P}} \left\| P_{\mathcal{I}_{i_1}} P_{\mathcal{I}_{i_2}} \cdots P_{\mathcal{I}_{i_k}} \right\|_2 \right)}.$$

Furthermore, if the rank of each subspace view is correctly estimated, i.e. $\text{rank}(\widehat{X}_k) = \text{rank}(X_k)$, then, the deviation of the estimated individual subspace from the true individual subspace is bounded by:

$$\|P_{\widehat{\mathcal{I}}_k} - P_{\mathcal{I}_k}\|_2 \leq 2 \dim(\mathcal{I}_k)^{1/2} \|R_{\mathcal{I}_k}\|_2.$$

Proof. We adapt the proof from Theorem 3.2 to the multi-view case. Both proofs rely on the version of the Davis-Kahan theorem of Yu et al. (2015).

Joint components. To apply Davis-Kahan theorem, we show that there exists an eigengap in the population-level model $S = \frac{1}{|\mathcal{P}|} \sum_{(i_1, i_2, \dots, i_k) \in \mathcal{P}} P_{\text{col}(X_{i_1})} P_{\text{col}(X_{i_2})} \cdots P_{\text{col}(X_{i_k})}$. Similar to Section 3.1, we use the orthogonality assumption $\mathcal{J} \perp \mathcal{I}_k$ to obtain $S = P_{\mathcal{J}} + \frac{1}{|\mathcal{P}|} \sum_{(i_1, i_2, \dots, i_k) \in \mathcal{P}} P_{\mathcal{I}_{i_1}} P_{\mathcal{I}_{i_2}} \cdots P_{\mathcal{I}_{i_k}}$. Fix an orthonormal basis, $U_{\mathcal{J}}$, for $P_{\mathcal{J}}$. Since $\mathcal{J} \perp \mathcal{I}_k$, we have that $S U_{\mathcal{J}} = U_{\mathcal{J}}$. Hence, S has at least $\dim \mathcal{J}$ eigenvalues that are equal to 1 with corresponding eigenvectors forming \mathcal{J} . Now fix any orthonormal vector $u \in \text{span } U_{\mathcal{J}}^{\perp}$. Then we have:

$$\begin{aligned} \|S u\|_2 &= \left\| P_{\mathcal{J}} u + \frac{1}{|\mathcal{P}|} \sum_{(i_1, i_2, \dots, i_k) \in \mathcal{P}} P_{\mathcal{I}_{i_1}} P_{\mathcal{I}_{i_2}} \cdots P_{\mathcal{I}_{i_k}} u \right\|_2 \\ &\leq \frac{1}{|\mathcal{P}|} \sum_{(i_1, i_2, \dots, i_k) \in \mathcal{P}} \left\| P_{\mathcal{I}_{i_1}} P_{\mathcal{I}_{i_2}} \cdots P_{\mathcal{I}_{i_k}} \right\|_2 && \text{(by triangle-inequality)} \\ &< 1. && \text{(since } \bigcap \mathcal{I}_k = \{\mathbf{0}\}) \end{aligned}$$

Therefore, the spectrum of S becomes $\sigma_r(S) = 1$ for $1 \leq r \leq \dim \mathcal{J}$ and $\sigma_r(S) < 1$ for $r > \dim \mathcal{J}$.

From here, applying Davis-Kahan, we have that:

$$\|\sin \Theta(U_{\widehat{\mathcal{J}}}, U_{\mathcal{J}})\|_2 \leq \frac{2 \dim(\mathcal{J})^{1/2} \|\widehat{S} - S\|_2}{1 - \frac{1}{|\mathcal{P}|} \sum_{(i_1, i_2, \dots, i_k) \in \mathcal{P}} \left\| P_{\mathcal{I}_{i_1}} P_{\mathcal{I}_{i_2}} \cdots P_{\mathcal{I}_{i_k}} \right\|_2}$$

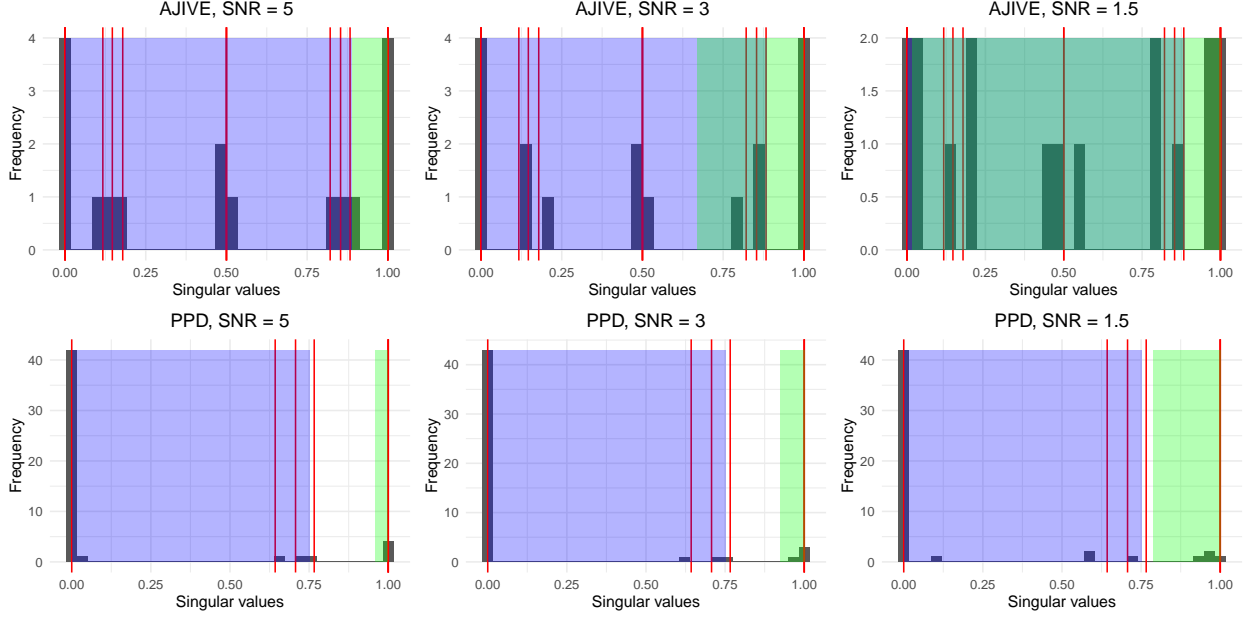


FIGURE 4. Simulated data of § 4 with angle $\phi = 40^\circ$ and varying SNR. **Top row:** Spectrum of \hat{S}_{sum} analyzed by AJIVE (Feng et al., 2018). **Blue region** indicates the noise bound; **green region** indicates the joint Wedin bound, both computed using bootstrap. **Bottom row:** Spectrum of \hat{M} analyzed in our approach. **Blue region** indicates the noise bound from (5); **green region** indicates the joint bound computed using bootstrap from (4). For both rows, **red lines** indicate the true spectrum of S_{sum} and M , respectively.

Putting everything together, we have:

$$\begin{aligned}
\|P_{\hat{\mathcal{J}}} - P_{\mathcal{J}}\|_2 &= \|\sin \Theta(U_{\hat{\mathcal{J}}}, U_{\mathcal{J}})\|_2 \\
&\leq \frac{2 \dim(\mathcal{J})^{1/2} \|\hat{S} - S\|_2}{1 - \frac{1}{|\mathcal{P}|} \sum_{(i_1, i_2, \dots, i_k) \in \mathcal{P}} \|P_{\mathcal{I}_{i_1}} P_{\mathcal{I}_{i_2}} \dots P_{\mathcal{I}_{i_k}}\|_2} \\
&\leq \frac{2 \dim(\mathcal{J})^{1/2} \left\| \sum_{\mathcal{S} \subset \{1, 2, \dots, K\}} \prod_{j=1}^K W_{i_j}(\mathcal{S}) \right\|_2}{|\mathcal{P}| \left(1 - \frac{1}{|\mathcal{P}|} \sum_{(i_1, i_2, \dots, i_k) \in \mathcal{P}} \|P_{\mathcal{I}_{i_1}} P_{\mathcal{I}_{i_2}} \dots P_{\mathcal{I}_{i_k}}\|_2 \right)},
\end{aligned}$$

where $W_{i_j}(\mathcal{S}) = P_{\text{col}(X_{i_j})}$ if $i_j \in \mathcal{S}$ and $W_{i_j}(\mathcal{S}) = \Delta_{i_j}$ otherwise.

Individual components. The case for individual components is the same as in Theorem 3.2. \square

A.4. Detailed comparison with related methods. Our approach builds on the principal angle formulation by analyzing the product of projections, which directly reveals subspace alignment. This formulation was first explored for multi-view data in Feng et al. (2018), where the authors instead studied the sum of the projection matrices $S_{sum} = (P_{\text{col}(X_1)} + P_{\text{col}(X_2)})/2$ rather than the product. Applying Lemma 2.1 to the sum gives

$$S_{sum} = P_{\mathcal{J}} + P_{\mathcal{O}_1}/2 + P_{\mathcal{O}_2}/2 + (P_{\mathcal{N}_1} + P_{\mathcal{N}_2})/2,$$

which reveals that its spectrum has $\dim(\mathcal{J})$ eigenvalues equal to 1 with eigenvectors corresponding to joint subspace, $\dim(\mathcal{O}_1) + \dim(\mathcal{O}_2)$ eigenvalues equal to 1/2 with eigenvectors corresponding to orthogonal individual subspaces, and $\dim(\mathcal{N}_1) + \dim(\mathcal{N}_2)$ eigenvalues of the form $\{\sigma_i\}^2 = \{1 \pm \cos(\phi_i)\}/2$, where ϕ_i are $\dim(\mathcal{N}_1)$ principal angles between non-orthogonal \mathcal{N}_1 and \mathcal{N}_2 . The gap separating joint from individual subspaces is of the size $\{1 - \sigma_{\max}(\Sigma)\}/2$. In contrast, $P_{\text{col}(X_1)}P_{\text{col}(X_2)}$ has only $\dim(\mathcal{J}) + \dim(\mathcal{N}_1)$ non-zero singular values, and the gap separating joint from individual subspaces is twice larger, $\{1 - \sigma_{\max}(\Sigma)\}$.

The above comparison of the population quantities directly affects the resulting estimation. Since in practice only estimates $\text{col}(\hat{X}_1)$ and $\text{col}(\hat{X}_2)$ are available, the resulting \hat{S}_{sum} and $P_{\text{col}(\hat{X}_1)}P_{\text{col}(\hat{X}_2)}$ both have perturbed spectrum. Since S_{sum} has a smaller spectral gap between joint and individual subspaces, and a larger number of non-zero singular values unrelated to joint structure $\dim(\mathcal{O}_1) + \dim(\mathcal{O}_2) + \dim(\mathcal{N}_1) + \dim(\mathcal{N}_2)$, \hat{S}_{sum} is more affected by noise perturbations than $P_{\text{col}(\hat{X}_1)}P_{\text{col}(\hat{X}_2)}$. As shown in Figure 4, the singular values from Feng et al. (2018) do not exhibit the clustering observed in our method.

Furthermore, estimating joint structure based on the product of projections has advantages beyond rank estimation. To illustrate this, consider the symmetrized version

$$\hat{S} = (P_{\text{col}(\hat{X}_1)}P_{\text{col}(\hat{X}_2)} + P_{\text{col}(\hat{X}_2)}P_{\text{col}(\hat{X}_1)})/2.$$

The two objects are related as $2\hat{S}_{sum}^2 - \hat{S}_{sum} = \hat{S}$. Therefore, non-trivial eigenvectors of \hat{S} are also non-trivial eigenvectors of \hat{S}_{sum} . However, eigenvectors of \hat{S}_{sum} with eigenvalue 1/2 are in the null space of \hat{S} . In principle, these eigenvectors of \hat{S}_{sum} correspond to the individual orthogonal directions in \mathcal{O}_1 and \mathcal{O}_2 , or specifically $\text{col}(\hat{X}_1) \cap \text{col}(\hat{X}_2)^\perp$ or $\text{col}(\hat{X}_1)^\perp \cap \text{col}(\hat{X}_2)$. Our proposed estimate of joint structure automatically excludes such directions.

We further provide a more detailed comparison between the proposed approach and the method of Feng et al. (2018) using angle $\phi = 40^\circ$ and varying SNR $\in \{1, 3, 5\}$. One key advantage of the proposed algorithm is the diagnostic plot, which could be used to assess the quality of joint rank estimation in practice. The bottom row of Figure 4 illustrates these diagnostic plots by showing the spectrum of $P_{\text{col}(\hat{X}_1)}P_{\text{col}(\hat{X}_2)}$ together with the proposed bootstrap bound $1 - \hat{\varepsilon}_1$ (obtained in step 2 of Algorithm 1) and noise bound λ_+ (obtained in step 3 of Algorithm 1). Observe that singular values cluster into groups corresponding to joint, non-orthogonal individual and remaining directions. In the high signal-to-noise ratio, our bootstrap bound for joint directions effectively identifies the corresponding top cluster, leading to the correct estimate of the joint rank as 4. Furthermore, the noise bound and the bootstrap bound do not overlap. In contrast, when signal-to-noise is low, the bootstrap bound becomes loose due to the increased error in subspace estimation (hence inflated Δ_k in (4)). Here, the noise bound compensates by filtering out rotated directions since their deteriorated alignment disqualifies them from being included as a joint signal. In comparison, the top row of Figure 4 illustrates the spectrum of $P_{\text{col}(\hat{X}_1)} + P_{\text{col}(\hat{X}_2)}$ used by AJIVE (Feng et al., 2018). The lack of clustering in the spectrum makes the separation of joint directions more challenging. Like our approach, Feng et al. (2018) uses the maximum of two bounds to determine joint rank: bootstrap estimate of the Wedin bound to identify the joint structure and bootstrap bound to filter out the noise directions. Figure 4 shows that our joint bound is tighter since the noise bound of Feng et al. (2018) almost always dominates the joint bound. We believe that the tightness of our joint bound is due to taking explicit advantage of perturbation ε_1 in Theorem 3.1 when performing bootstrap. In terms of noise bound, the two approaches agree in values, differing by at most 2% on average across simulations, but the main difference is that our bound λ_+ is analytical based on random matrix theory whereas Feng et al. (2018) estimate it using the bootstrap. Overall, Figure 4 suggests that improved performance of proposed method is due to a more clear separation of joint directions in the spectrum of $P_{\text{col}(\hat{X}_1)}P_{\text{col}(\hat{X}_2)}$ compared to the spectrum of $P_{\text{col}(\hat{X}_1)} + P_{\text{col}(\hat{X}_2)}$, as well as tighter bound that we use to identify this separation in practice.

APPENDIX B. ADDITIONAL EXPERIMENTS

B.1. Simulations on synthetic data for more than two views. Similar to Section 4, we run simulations for the case of 3 views under various rank corruption, signal-to-noise ratio, and angles. We set the joint ranks to be $\text{rank}(J_k) = 3$, and the ranks of the individual subspaces to $\text{rank}(I_1), \text{rank}(I_2), \text{rank}(I_3)$. We take the matrix dimensions to be $n = 35$ and $p_1 = 40, p_2 = 45, p_3 = 50$. We report our results in Table 4. From the table, we see that our method consistently performs in the top among other methods. In addition, we note that the proposed approach offers strong performance even under the more difficult conditions such as low signal-to-noise ratio and highly rotated angles.

B.2. Ablation study for bootstrap. We modify the bootstrap method proposed in Prothero et al. (2024) to better align the resampled singular vector bases with the observed data. Specifically, given orthogonal resampled bases $U_{1,(b)}$ and $U_{2,(b)}$, we adjust $U_{2,(b)}$ to align with $U_{1,(b)}$ using the formula: $U_{2,(b)} \leftarrow$

TABLE 4. Quality of the joint and individual subspace estimates in terms of the metric (6), where larger values indicate better performance. All values are multiplied by 10. The results are averaged across 100 iterations. Maximum standard error of the mean is 0.03. We highlight the best result in **bold** and underline second best result. We denote by (*) methods that do not allow supplying marginal ranks for each view. We denote Lock et al. (2013) as JIV, Feng et al. (2018) as AJI, Gaynanova & Li (2019) as SLI, Park & Lock (2020) as UNI, and our method as PPD.

	Under-specified rank				Estimated rank				Over-specified rank			
	SNR = 2		SNR=0.5		SNR = 2		SNR=0.5		SNR = 2		SNR=0.5	
	90°	30°	90°	30°	90°	30°	90°	30°	90°	30°	90°	30°
JIV	-	-	-	-	9.08	7.49	4.81	4.55	-	-	-	-
AJI	8.67	7.77	6.04	5.69	<u>9.79</u>	<u>8.45</u>	3.81	3.63	<u>9.08</u>	<u>7.63</u>	6.21	5.91
SLI*	-	-	-	-	9.47	7.43	1.17	1.09	-	-	-	-
UNI*	-	-	-	-	9.04	8.08	<u>4.32</u>	<u>3.92</u>	-	-	-	-
PPD	<u>8.03</u>	<u>7.41</u>	<u>5.43</u>	<u>5.44</u>	9.83	9.75	3.70	3.64	9.12	9.07	<u>5.67</u>	<u>5.57</u>

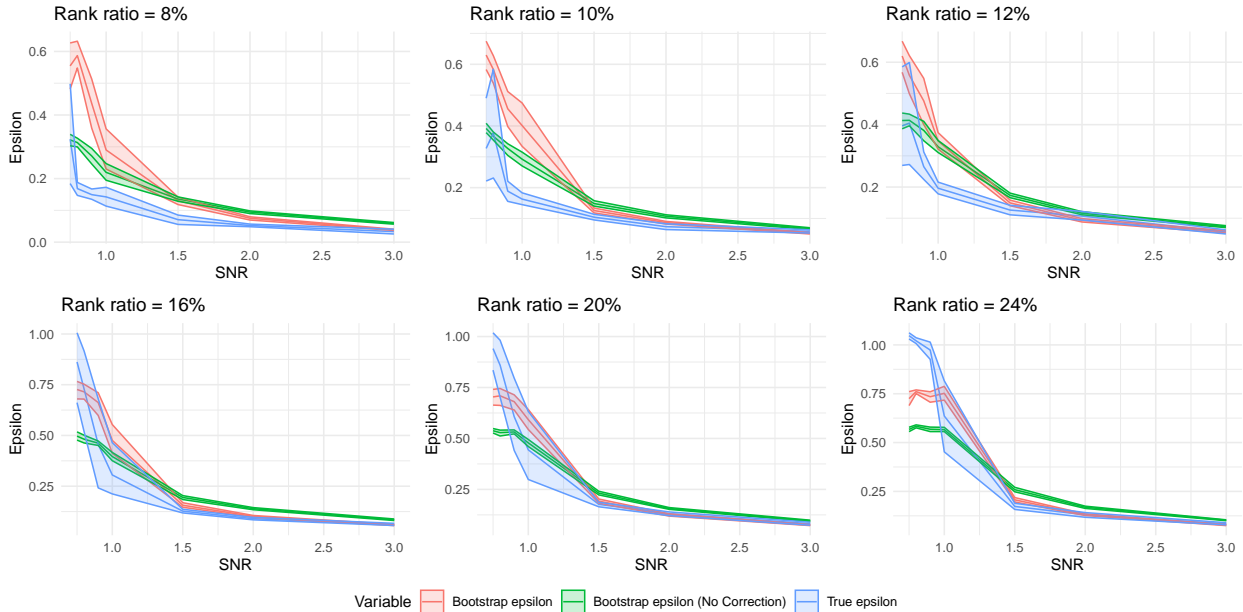


FIGURE 5. Estimate of ε_1 computed with and without our modification, aligning the view-specific bases. We simulate the data as in Section 4, fix the angle between individual subspaces at 60° , while varying the rank-to-dimension and signal-to-noise ratios. We produce the confidence intervals based on 10 re-runs.

$U_{1,(b)} \cos(\Sigma_{\widehat{M}}) + U_{2,(b)} \sin(\Sigma_{\widehat{M}})$, where $\Sigma_{\widehat{M}}$ is a diagonal matrix containing the principal angles between the column spaces $\text{col}(\widehat{X}_1)$ and $\text{col}(\widehat{X}_2)$. This alignment ensures that the resampled bases reflect the geometric relationship observed in the data, which is crucial for accurate estimation of ε_1 and ε_2 . Without this correction, a straightforward approach would be to randomly sample $U_{1,(b)}$ and $U_{2,(b)}$ from the Haar measure. However, as we argue in Section 3.3, such an approach tends to underestimate ε_1 and ε_2 , particularly when the rank-to-dimension ratio is low. In this regime, randomly sampled bases are likely to be nearly orthogonal, which does not capture the true alignment between the column spaces of \widehat{X}_1 and \widehat{X}_2 .

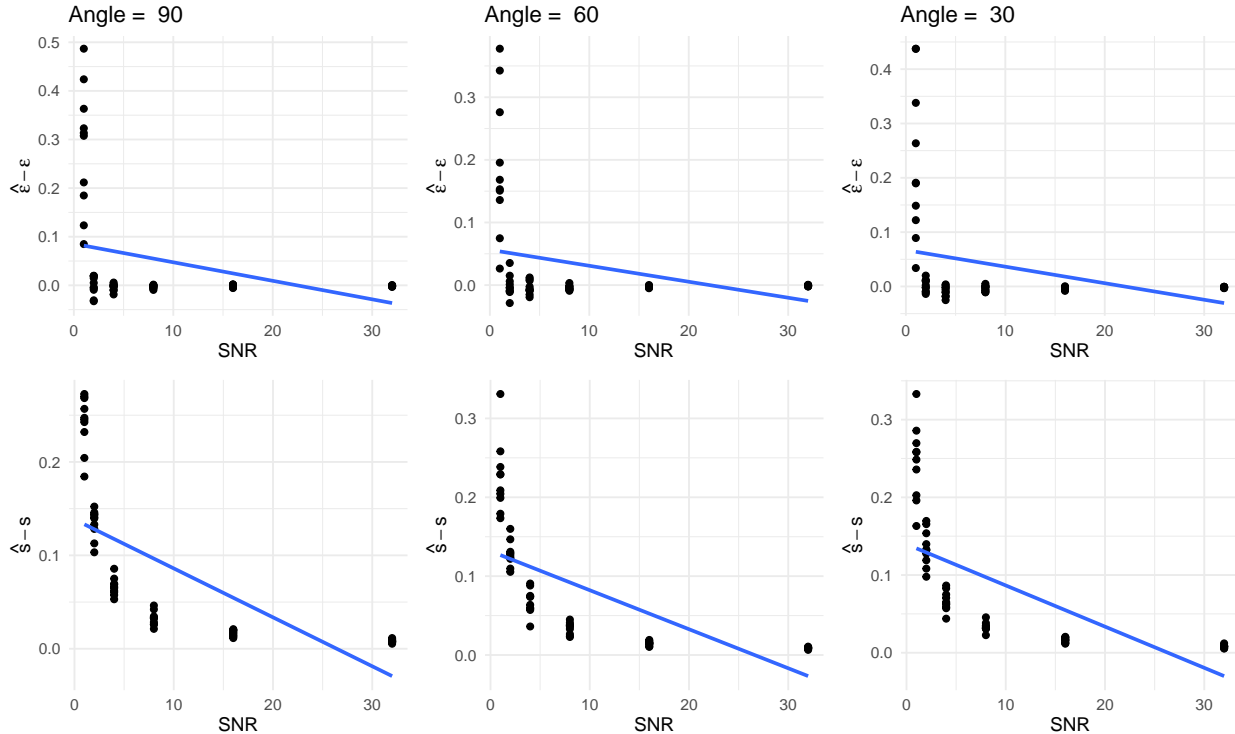


FIGURE 6. **Top row:** Error in the bootstrap estimate of ϵ_1 . **Bottom row:** error in the noise variance estimation by the robust estimator y_{med}/μ_β .

We investigate the effect of our correction in Figure 5 for ϵ_1 with similar conclusions holding for ϵ_2 . To generate the figure, we simulate data following the procedure in Section 4, fixing the angle between individuals at 60° while varying the rank-to-dimension and signal-to-noise ratios. The 95% confidence intervals are computed using 10 re-runs.

From the figure, we observe that our corrected bound provides better control over the true ϵ_1 , offering more accurate coverage in the low signal-to-noise ratio regime and tighter bounds in the high signal-to-noise ratio regime. Recall that $\epsilon_1 := \|P_{\text{col}(X_1)}(\Delta_1 + \Delta_2 + \Delta_1\Delta_2)P_{\text{col}(X_2)}\|_2$. The projection operators $P_{\text{col}(X_1)}$ and $P_{\text{col}(X_2)}$ reduce the estimate by filtering out components of the error terms that lie within the column spaces of X_1 and X_2 , respectively. Recall from Figure 7, for random projections $P_{\text{col}(X_1)}$ and $P_{\text{col}(X_2)}$, the spectral density depends on the rank-to-dimension ratios: the bulk of singular values is around zero, with the tail extending towards one as the rank-to-dimension ratio increases. Hence, the naive estimate tends to underestimate ϵ_1 , especially when the rank-to-dimension ratio is low, because the resampled projections $P_{\text{col}(X_1)}$ and $P_{\text{col}(X_2)}$ are nearly orthogonal, causing more directions to be filtered out. This effect is more pronounced for low signal-to-noise ratios, as the error terms Δ_k are larger. We note that our corrected bound tends to be tighter in the high signal-to-noise ratio regime, and we leave a detailed investigation of this phenomenon for future work.

B.3. Empirical error of the bootstrap. We simulate the data following Section 4, setting. We run our bootstrap model for a range of signal-to-noise ratios and angles, supplying the model with the true marginal ranks. We report the difference $\hat{\epsilon}_1 - \epsilon_1$ in Figure 6. From the figure, we see that our bootstrap estimator tends to be accurate, except for the low signal-to-noise ratios for which it overestimates the true parameter. We investigate this issue and find it related to the overestimation of the noise variance by the robust estimator y_{med}/μ_β with $y_{\text{med}}, \mu_\beta$ denoting the median singular value of Y and the median of the Marchenko-Pastur distribution with parameter β . We show the error in the variance estimation in Figure 6. Recall that in our bootstrap as described in Section 3.3, we impute the signal directions back into the noise estimate \check{E}_k , which are scaled by the noise variance. As our estimate of the noise variance overestimates the

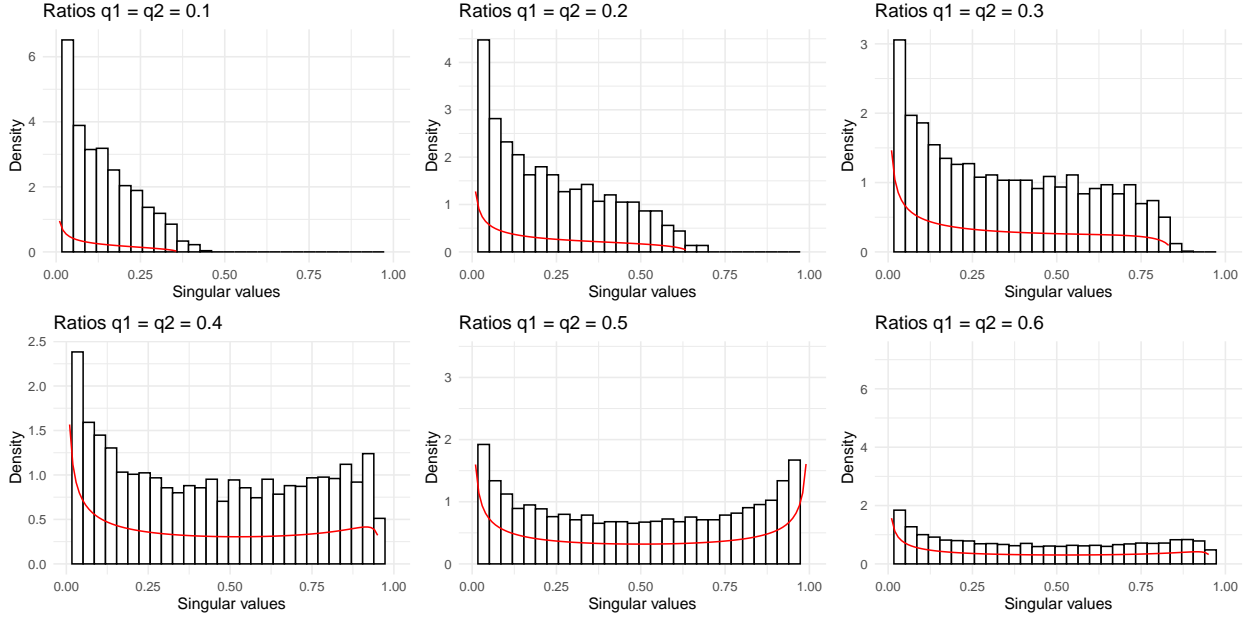


FIGURE 7. Asymptotic distribution of the spectrum of the product of two random projections, parametrized by the subspace-to-ambient dimension ratios $q_1 = r_1/n$ and $q_2 = r_2/n$.

truth, correspondingly our noise estimate becomes inflated, which finally leads to the inflated $\hat{\varepsilon}_1$ estimate. We leave the improvement of our bootstrap estimator in the low signal-to-noise ratio regime as future work.

B.4. Asymptotic distribution of spectrum of random projections. To simulate the spectrum of two random projection matrices, we sample orthonormal bases U_1 and U_2 of ranks r_1 and r_2 from the Haar measure. We set the ambient dimension to $n = 100$. We then compute the squares of the singular values of the matrix $U_1^\top U_2$. In Figure 7, we present the histogram of these squares, λ , overlaid with the continuous part of the asymptotic density provided in Equation (5).